Persistent cortical excitatory neuron dysregulation in adult *Chd8* haploinsufficient mice.

Cesar P. Canales*[1,2,3], Stephanie A. Lozano*[1], Nicholas A. Frost[6], Karol Cichewicz[1, 2], Wellington Amaral[3], Nicolas Seban[1], Ethan Fenton[1], Ayanna Wade[1], Nickolas Chu[1], Emily Smith[1], Cory Ardekani[1], Samuel Frank[3], Jeffrey Bennett[3], Pierre Lavenex[4], Aspen Kopley-Smith[1], Darlene Rahbarian[1], Melissa Corea[1], Daniela Perla[1], Liam Davis[1], Jiyuan Zhu[1], Rebecca Ortiz[1], Paris Beauregard[1,2], Sarah Morse[1], , Jacob Baker[5], Jingqi Sun[5], Boxuan Ma[5], Ju Lu[5,8], Vikaas S. Sohal[7], David G. Amaral[1,2,3], Yi Zuo[5], Alex S. Nord[1,2,3]

Affiliations:

1) UC Davis Center for Neuroscience, Davis, CA 95618, USA

2) Department of Psychiatry and Behavioral Sciences, University of California Davis, Sacramento, CA 95817, USA

3) The M.I.N.D. Institute, UC Davis, Sacramento, CA, USA

4) Laboratory of Brain and Cognitive Development, Institute of Psychology, University of Lausanne, Switzerland

5) Department of Molecular, Cell and Developmental Biology, University of California Santa Cruz, Santa Cruz, CA 95064, USA

6) University of Utah, Department of Neurology, Salt Lake City, Utah, United States of America

7) Department of Psychiatry and Behavioral Sciences, University of California, San Francisco | Weill Institute for Neurosciences, University of California, San Francisco | Kavli Institute for Fundamental Neuroscience, University of California, San Francisco

8) Present address: Department of Biological Sciences, Lehigh University, Bethlehem, PA 18015, USA

* These authors contributed equally

Abstract

CHD8 mutations cause autism spectrum disorder, cognitive deficits, and macrocephaly. *Chd8*$^{+/-}$ mouse models exhibit macrocephaly and transcriptional pathology, with inconsistent findings regarding neurogenesis, neuron function, and behavior. Via stereology and single nucleus transcriptomics (snRNA-seq), we found increased *Chd8*$^{+/-}$ cortical volume was not explained by increase in neuron number. Differential expression (DE) was present across cortical cell types, with excitatory neurons exhibiting high DE burden and shared and subclass-specific DE signatures. Bulk RNA-seq DE of constitutive *Chd8*$^{+/-}$ and conditional *Camk2a-Cre Chd8*$^{+/-}$ mice identified shared transcriptional pathology. DE in synaptosomal versus nuclear mRNA identified overlapping DEGs, but also significant differences and exaggerated synaptosomal changes. Building on DE findings implicating glutamatergic neurons, we found *Chd8*$^{+/-}$ mice exhibited altered excitatory neuron spine density and dynamics, decreased GCaMP activity correlation, and sleep perturbation. Thus, *Chd8* haploinsufficiency causes lasting excitatory neuron dysfunction, perturbs RNA regulation beyond transcription, and impacts neuronal properties, cortical microcircuits, and behavior.

Introduction

Mutations in a growing list of genes cause Neurodevelopmental Disorders (NDDs) with overlapping but complex presentation, including autism spectrum disorder (ASD), intellectual disability (ID), and behavior or psychiatric disorders[1,2]. *CHD8* encodes the chromatin remodeling factor (CRF) Chromodomain Helicase DNA-binding protein 8, and has among the highest rates of protein disrupting rare and de novo mutations in ASD cases[1]. CHD8-associated NDD (*CHD8*-NDD) has core but variably expressed features including ASD, ID, and macrocephaly, as well as sleep, gastrointestinal, psychiatric, and neurological issues[3–9]. Clarifying the links between *CHD8* haploinsufficiency, macrocephaly, and pathology may offer critical insights into the etiology of the 15% of ASD patients that exhibit more severe cognitive and behavioral phenotypes often with poorer prognosis[10]. Furthermore, CHD8 has been identified as a central regulator in network studies of ASD-associated loci[11–13], and serves as a key example of the many CRF genes implicated in ASD and other NDDs[14–18]. Defining the pathological consequences associated with *CHD8* haploinsufficiency is thus an important step towards understanding both *CHD8*-specific mechanisms and broader NDD neurobiology.

Chd8 is ubiquitously expressed and knockout is embryonic lethal in mice[19,20]. NDD-relevant phenotypes have been observed across studies of heterozygous *Chd8*$^{+/-}$ mouse models[20–26]. Among the consistent findings across constitutive *Chd8*$^{+/-}$ mouse models is the presence of adult macrocephaly and transcriptional pathology[20,22,24,25]. Bulk RNA-seq on developing and adult *Chd8*$^{+/-}$ mouse brain has been performed in a number of studies, finding relatively subtle effects but replicated perturbation of energetics and protein homeostasis and downregulation of synaptic and neuronal genes[20,21,24,25,27–30]. Recent single cell studies of *Chd8*$^{+/-}$ mice suggest subtle changes in neurodevelopment and perturbations to neurons[31–33], but have lacked resolution to analyze specific subtypes in mature cortex. Studies of *Chd8*$^{+/-}$ mouse behavior and cognition have been more variable[20–26], with evidence that some variability is due to genetic background[34,35]. Multiple studies of *Chd8* haploinsufficiency have identified changes to electrophysiology in the cortex and in in vitro[21,24,36,37], indicating impacts on neuron function. In vitro studies in human and non-human primate neurons and human cortical organoids also

68 indicate perturbation to neurogenesis, increases in organoid size paralleling macrocephaly, and
69 neuronal electrophysiological and network level dysfunction[31,32,38–41]. Finally, conditional *Chd8* knockout
70 studies have been conducted targeting specific cell types such as excitatory neurons[36,42–46],
71 oligodendrocytes[47–49], and astrocytes and microglia[50,51]. Many of these studies have primarily focused
72 on homozygous conditional mutants, which may not accurately model the heterozygous mutations
73 relevant to NDDs.

74 Despite extensive study of *Chd8* as a representative ASD/NDD risk gene, key questions remain
75 regarding how heterozygous mutation leads to pathology at the cellular, molecular, and circuit level.
76 First, no published studies have linked adult macrocephaly to changes in cellular composition or
77 described cell-type specific molecular pathology in adult *Chd8*$^{+/-}$ mouse brain. Second, it remains
78 unclear whether neuronal dysfunction has arisen from developmental disruption or reflects a continued
79 requirement for full *Chd8* dosage in mature neurons, and whether reported RNA expression changes
80 are due to transcriptional or post-transcriptional mechanisms. Third, circuit-level consequences to
81 behavior beyond sociability and cognition remain largely unexplored. To address these gaps, we
82 characterized adult *Chd8*$^{+/-}$ mice and cerebral cortex across cellular, molecular, functional, and
83 behavioral domains (**Figure 1A**). Our findings reveal selective vulnerability of cortical glutamatergic
84 neurons to *Chd8* haploinsufficiency, implicate disrupted post-transcriptional regulation of synaptosomal
85 RNA homeostasis, and demonstrate associated changes in dendritic spine dynamics, impaired
86 neuronal signaling coherence, and altered sleep architecture in *Chd8*$^{+/-}$ mice.

87 **Results**

88 *Description of Chd8 mutant mouse lines*

89 Constitutive mutant *Chd8* mice were generated on the C57BL/6N background via CRISPR/Cas9
90 targeting exon 5, resulting in a 5 bp deletion that leads to reduced *Chd8* mRNA and protein and is early
91 embryonic homozygous lethal. We previously characterized heterozygous mutants from this line
92 (referred to as *Chd8*$^{+/5bpdel}$, herein *Chd8*$^{+/-}$), reporting differential expression and splicing, altered cortical

93 proliferation, increased brain volume, and phenotypes of altered exploration in open field assay and
94 deficits in fear conditioning and novel object recognition[20]. We also use a conditional *Chd8* loxP mutant
95 on the C57BL/6J background generated by Jackson Laboratory where exon 3 is ablated in the
96 presence of CRE (*Chd8*^{em3Lutzy}). These were mated to *Camk2a*-CRE (B6.Cg-Tg(Camk2a-cre)T29-
97 1Stl/J; JAX strain: 005359) to direct conditional heterozygous ablation in post-mitotic forebrain
98 glutamatergic neurons in this line, herein referred to as *Chd8*$^{+/flox}$.

99 *Increased adult cortical volume without increase in neuron number or soma size in Chd8*$^{+/-}$ *mice*

100 We previously identified increased cortical volume and macrocephaly in *Chd8*$^{+/-}$ mice via structural
101 MRI[20]. Here, we aimed to replicate this finding and determine whether the volume increase results from
102 a higher number of neurons. We performed unbiased stereological analysis on Nissl-stained brain
103 sections from male and female heterozygous *Chd8*$^{+/-}$ mice and wild-type littermates at postnatal day 42
104 (P42) (**Figure 1B-C**), an age marking the end of adolescence and a mature stage of mouse brain
105 development[52]. We examined 15–18 representative coronal sections per mouse using established
106 stereological methods to accurately assess cortical volume, neuronal distribution, and soma size.
107 Cortical volume was estimated using the Cavalieri method[53,53,54], revealing a significant overall increase
108 in *Chd8*$^{+/-}$ mice compared to wild-type littermates (**Figure 1D**, P=0.032, Student's t-test). When
109 stratified by sex, the increase in cortical volume was more pronounced and independently significant in
110 males (P=0.009 males; P=0.61 females, Student's t-test). Comparing volume across rostral-caudal
111 sections, *Chd8*$^{+/-}$ males showed increase in more rostral regions (**Figure S1A**).

112 Next, we investigated whether the cortical volume expansion was associated with an increase in
113 neuronal numbers or soma size. Using the optical fractionator method[55], we estimated neuron counts
114 across the cortex. We did not find significant differences in total neuron number in either the full cohort
115 or sex-stratified analyses (P=0.76, unstratified; P=0.37, males; P=0.3, females) (**Figure 1E**). Finally, we
116 assessed neuronal soma size and found no significant differences between genotype groups in full or
117 sex-stratified analyses (P=0.23, unstratified; P=0.81, males; P=0.19, females) (**Figure S1B**). Taken

together, these findings replicate the cortical volume increase observed in *Chd8*$^{+/-}$ mice, with a stronger effect in males, and demonstrate that this expansion is not explained by an increase in neuronal number or soma size. Instead, the increased cortical volume without an increase in numbers results in decreased glutamatergic neuron density in the *Chd8*$^{+/-}$ cortex.

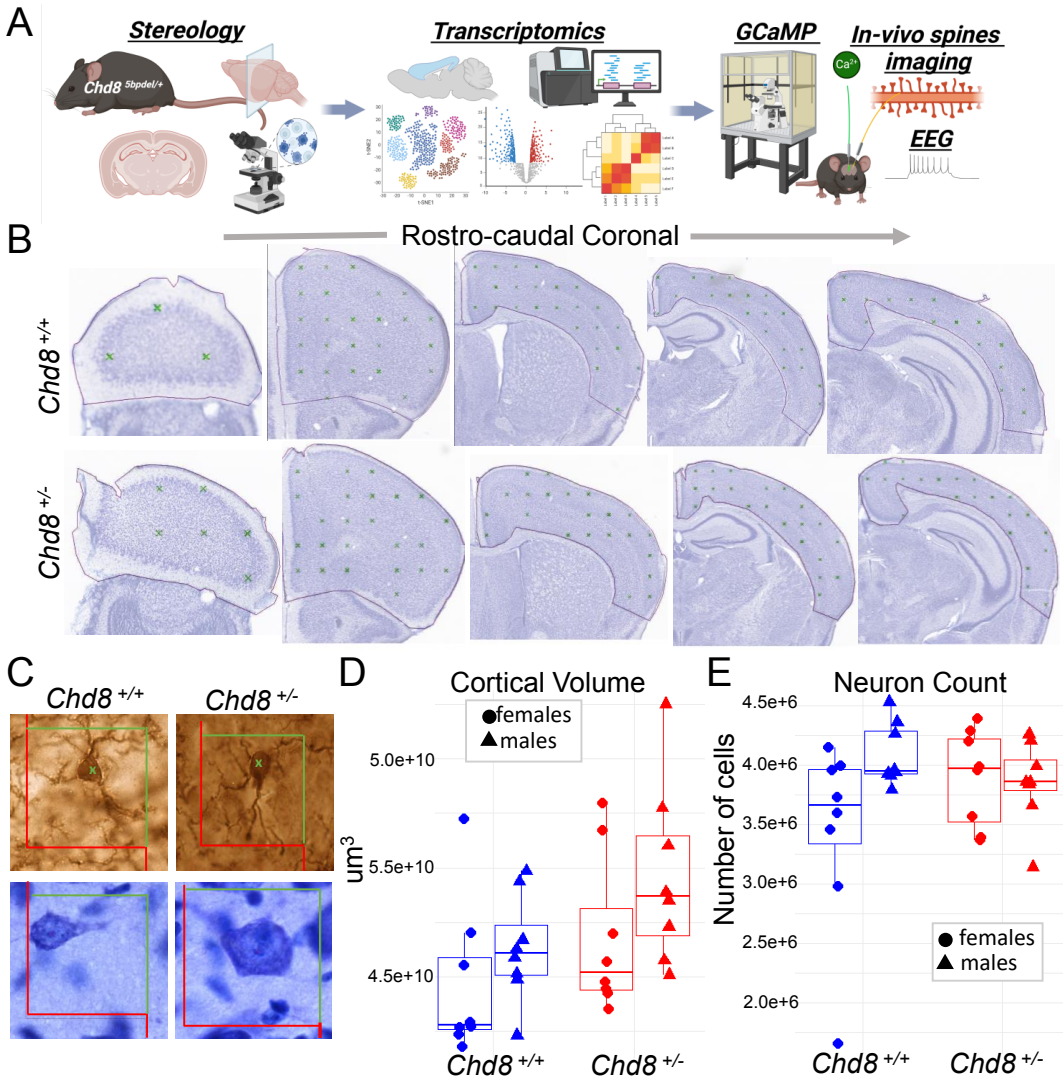

Figure 1. Increased cortical volume in *Chd8*$^{+/-}$ mice without a corresponding increase in neuron number. (A) Schematic overview of study investigating the role of *Chd8* haploinsufficiency in mature mouse cortex. (B–C) Representative coronal sections across the rostro-caudal extent of the cerebral cortex used for unbiased stereological analysis. (B) Cortical boundaries as determined for volume measurements. (C) Cellular organization visualized using Nissl staining (top) and NeuN immunostaining (bottom) in *Chd8*$^{+/+}$ and *Chd8*$^{+/-}$ mice. (D–E) Stereological profiles across the Z-plane showing (D) cortical volume estimates based on the Cavalieri method and (E) total neuron number as assessed by unbiased stereology in the same rostro-caudal regions. Data are stratified by sex and genotype. Error bars represent SEM. Statistical comparisons were performed using two-way ANOVA (Cortical volume: P=0.032 unstratified, P=0.009 males; P=0.61 females; Neuron Count: P=0.76, unstratified; P=0.37, males; P=0.30, females Student's t-test, N = 8 per sex/genotype).

134 *Cell-type specific cellular and molecular pathology in Chd8$^{+/-}$ P60 cortex*

135 Towards characterizing differences in RNA expression associated with *Chd8* haploinsufficiency in adult
136 (P60) mouse cortex, we performed single nucleus RNA sequencing (snRNA-seq) on constitutive
137 *Chd8$^{+/-}$* mice, as well as bulk RNA-seq on *Chd8$^{+/-}$* and conditional *Camk2a-CRE Chd8$^{+/flox}$* mutants, and
138 for nuclear and synaptosomal RNA from *Chd8$^{+/-}$* mutants (**Figure 2A**). For snRNA-seq, we analyzed
139 *Chd8$^{+/-}$* (male n = 3, female n= 2) and WT littermates (male n=2, female n=3 WT). Following quality
140 control and ambient RNA correction[56] (**Figure S2A**), there were 11,751 and 12,169 nuclei from *Chd8$^{+/-}$*
141 and WT samples, respectively, which we mapped to 18 cortical cell types based on marker gene
142 expression and integration with the Brain Initiative Cell Census Network mouse brain atlas[57] (see
143 methods) (**Figure 2B** and **Figure S2B**). There was balanced representation of male and female
144 samples and *Chd8$^{+/-}$* and WT samples (**Figure 2C**). Expected major cortical cell types were identified
145 as shown by expression of marker genes (**Figure 2D**). Cell identity was split at three levels: cell type 3
146 representing general classes (e.g. glutamatergic neurons), cell type 2 associated with specific
147 canonical subtypes (e.g. L4/5 IT), and cell type 1 representing data-driven further sub-clustering of
148 subtypes (e.g. L4/5 IT Glut1). Following UMAP generation and cell type identification, we tested for
149 differences in the relative representation of different cell types, comparing cell type proportions between
150 *Chd8$^{+/-}$* and WT groups (**Figure 2E**). At the cell type 2 level, there was significant increase in OPC and
151 decrease in L6 IT, with trending increase in astrocytes and decrease in microglia. These findings are
152 consistent with the results from stereology, demonstrating that macrocephaly and increased cortical
153 volume in *Chd8$^{+/-}$* mice is not due to increase in number of glutamatergic neurons and further
154 suggesting that increased cortical volume is not explained by expansion of specific cell types.

155 Next, we performed cell-type specific differential expression (DE) analysis using a cluster-level
156 pseudobulk framework[58], where reads are from the relevant cell type are aggregated at the sample
157 level, followed by DE testing using DESeq2[59] with experimental batch included as a covariate. We
158 performed DE analysis at each level of cell type identity (**Tables S5-S7**), with a focus on cell type 2 for
159 results here. Comparing DE burden (defined as the number of total DE genes divided by genes passing

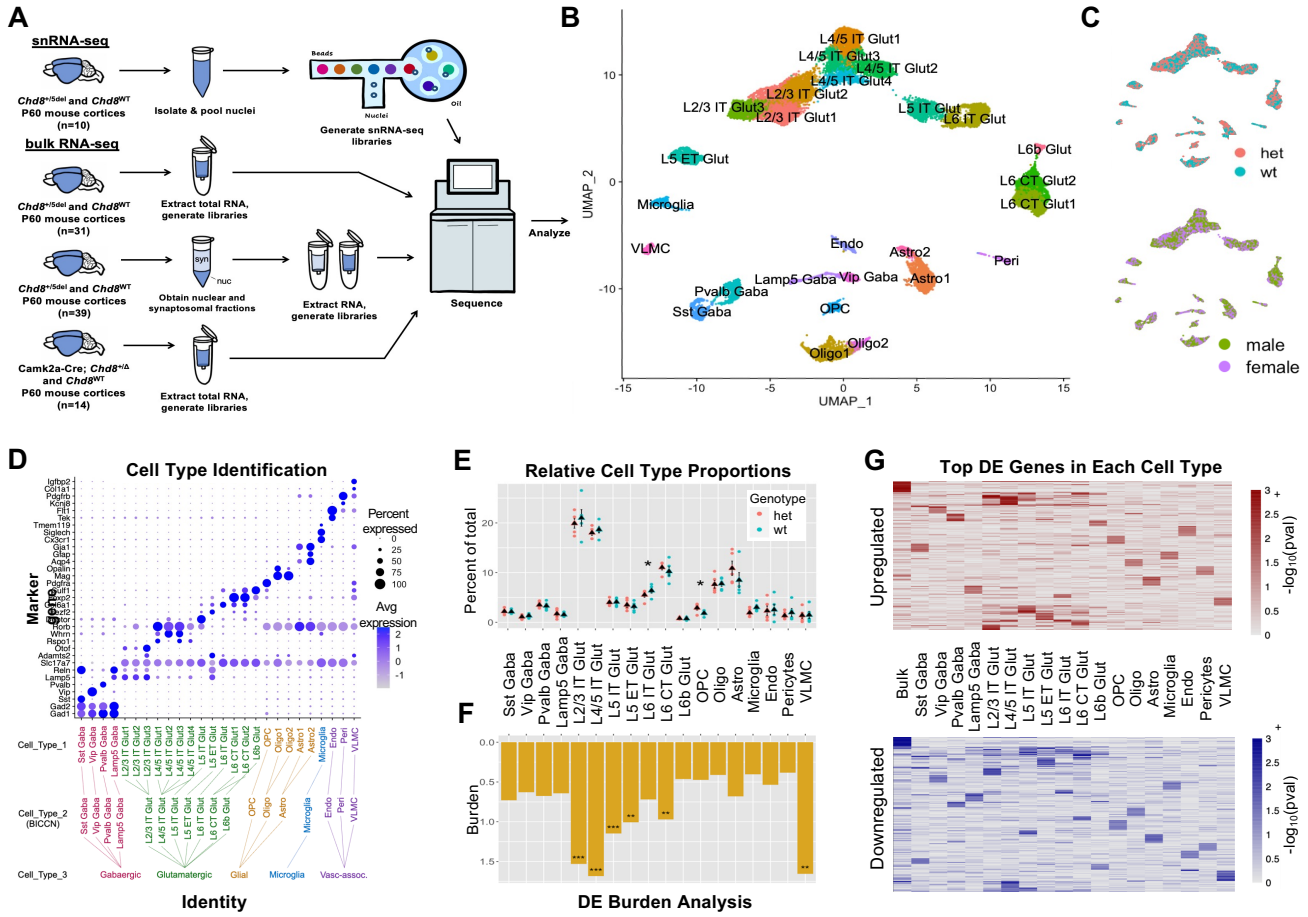

Figure 2: Cell type-specific pathology in adult *Chd8*$^{+/-}$ mouse cortex. A) Schematic depicting experimental design for RNA-seq and snRNA-seq experiments. B) UMAP of 23,920 cortical nuclei from P60 *Chd8*$^{+/-}$ and WT littermates with cell types annotated. C) Clustering of *Chd8*$^{+/-}$ (HET) and WT nuclei (top) and male and female nuclei (bottom) in UMAP space. D) Cell type identification dot plot representing average expression of cell type-specific marker genes in each cell type. Tree (bottom) shows 3 levels of cell type identification (Cell_Type_1-3). E) Cell type proportion comparison between *Chd8*$^{+/-}$ (HET) and WT nuclei, revealing a significant decrease in mutant L6 IT Glut nuclei (*p = 0.027) and increase in mutant OPCs (*p = 0.048) (Student's t-test). F) DEG burden across cell types (Burden = DE genes / expressed genes * 100). Significant DE burden was found in L2/3 IT (*p = 0.00001), L4/5 IT (*p = 0.00001), L5 IT (*p = 0.00001), L5 ET (*p = 0.0045), L6 CT Glut (*p = 0.0004), and VLMC (*p = 0.0009) nuclei (permutation test, n= 10,000). G) Heatmap showing –log10(pval) of top 25 unique upregulated (top) and downregulated (bottom) bulk and pseudobulk DEGs in each cell type (p < 0.1).

expression criteria for testing), glutamatergic cell types along with VLMC showed the largest impacts (**Figure 3F**). Among glutamatergic neurons, L2/3 intra-telencephalic (IT) and L4/5 IT neurons had the highest burden. DE results and burden were stable using either the full dataset or when down-sampling for equivalent cell/nuclei numbers across cell types and when using both uncorrected and ambient RNA corrected expression values, and similar differential expression effect direction and sizes were present

178 in stratified male and female samples (**Figure S2C-E**). At the single gene level, the top DE genes
179 (DEGs) varied by cell type, with the exception that glutamatergic neuron subtypes, showed
180 considerable overlap in effects (**Figure 3G**).

181 We performed gene set enrichment analysis (GSEA) based on DE rank using the clusterProfiler
182 package[60] (**Figure S2F**). Only glutamatergic neuron subtypes had DE signatures strongly associated
183 with GO terms (FDR < 0.05), with the strongest signatures in L2/3 IT and L4/5 IT. Using a relaxed
184 threshold of uncorrected P < 0.05, upregulated genes in glutamatergic neurons showed shared
185 enrichment for pathways including *Synapse organization*, *Synaptic signaling*, and *Axon guidance*, and
186 *Neuron differentiation*. Finally, we applied NeuronChat[61] to explore cell-cell communication networks
187 comparing receptor-ligand relationships in *Chd8*$^{+/-}$ and WT cortex based on snRNA-seq data (**Figure**
188 **S3**). This identified reduced Neurexin-Neuroligin interaction strength in *Cdh8*$^{+/-}$ mice, with the strongest
189 effect in L2/3 IT neurons (**Figure S3H-K**). At the level of information flow for individual receptor-ligand
190 pairs, NeuronChat identified a trend of increased information flow involving glutamate receptor-ligand
191 interactions in *Chd8*$^{+/-}$ mutants as well as decreased flow for specific Neurexin-Neuroligin pairs (**Figure**
192 **S3L**). These findings highlight disrupted synaptic signaling in *Chd8*$^{+/-}$ mice and suggest that
193 glutamatergic neuron subtypes, particularly L2/3 IT and L4/5 IT neurons, are disproportionately affected
194 in the adult cortex.

195 *Shared and cell-type specific DE co-expression modules in Chd8*$^{+/-}$ *glutamatergic neurons*

196 To capture systems-level expression patterns in glutamatergic neurons, we used hdWGCNA[61] to
197 identify gene co-expression modules and then identified differentially expressed modules (DEMs)
198 based on log2-transformed Fold Change (logFC) of module genes (see methods for details). All
199 glutamatergic cell subtypes were used as input to hdWGCNA, which yielded 10 modules accounting for
200 1,691 (17%) genes, with the remaining 8,115 genes assigned to the grey group (**Figure 3A-B, Table**
201 **S8**). 8/10 modules were DEMs in at least one glutamatergic subtype, as indicated by highlighted label
202 and box outlines in **Figure 3C-E.** Two modules (M1 and M7) were DEMs across most glutamatergic

203 subtypes, whereas the other six DEMs (M2, M3, M4, M6, M9, and M10) showed genotype differences
204 in only one or two subtypes. Module level differential expression direction and effect size varied, though
205 all but one DEM (M6 in L4/5 IT) were upregulated in *Chd8*$^{+/-}$ mutants. The modules varied in gene
206 number (**Figure 3B**) and relative expression patterns (**Figure 3C**) across glutamatergic subtypes and
207 cortical layers. The proportion of module genes that were individually DE (**Figure 3D, Figure S4A**) and
208 the module-level logFC (**Figure 3E**) similarly varied across modules and subtypes.

209 The glutamatergic co-expression modules showed different association to biological processes based
210 on GO enrichment (**Figure 3F**). First, 6/10 modules showed overlapping enrichment for a variety of
211 general neuron-associated terms (e.g. *Synapse assembly*, *Axon Guidance*, *Behavior*) without strong
212 module-specific GO terms. These included DEMs M1, M2, and M3, as well as non-DEMs M8 and M5.
213 These modules also exhibited differential expression across glutamatergic neuron subtypes and cortical
214 layers, suggesting that their co-expression is primarily driven by expression co-variation linked to cell
215 identity, rather than by shared biological pathways or genotype effects. The remaining four modules
216 (M4, M6, M7, M9) were all DEMs and featured strong module-specific GO enrichment: M4 and M9,
217 associated with *Aerobic Respiration* and *Translation* and upregulated in L2/3 IT, M6, associated with
218 *mRNA processing* and downregulated in L4/5 IT, and M7, which was broadly upregulated and
219 associated with general neuronal terms as well as GO terms represented by *Circadian rhythm*. In
220 addition to module-specific GO terms, these four modules did not show subtype- or laminar-associated
221 differences in relative expression and had DE signatures limited to individual glutamatergic subtypes.
222 We highlight gene-level differential expression patterns for DEMs of high interest in **Figure 3G**,
223 focusing on M1 and M7 modules that are broadly DE across glutamatergic subtypes, and M3 and M4
224 modules that are subtype-specific DEMs with prominent effects in L4/5 IT and L2/3 IT, respectively.
225 **Figure 3H** shows representative gene expression patterns from these DEMs visualized in UMAPs and
226 pseudobulk-level relative expression plots. See **Figure S4B-C** for extended modules visualizations. M1
227 (featuring *Rspo2*) includes a large set of genes that are expressed most highly in deep layer excitatory

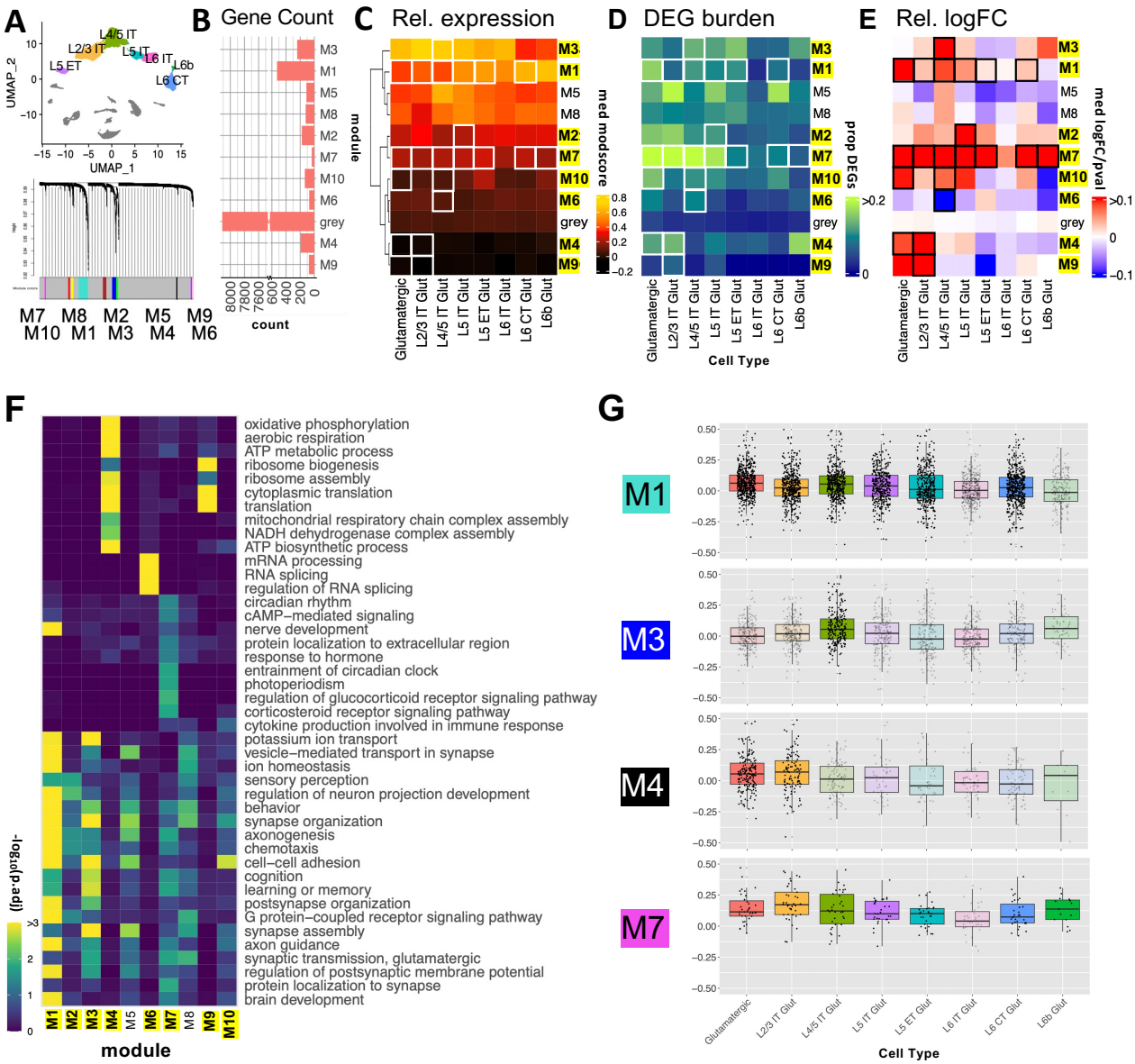
A
B Gene Count
C Rel. expression
D DEG burden
E Rel. logFC
F
G
M1
M3
M4
M7
Cell Type
module
count
med modscore
prop DEGs
med logFC/pval
oxidative phosphorylation
aerobic respiration
ATP metabolic process
ribosome biogenesis
ribosome assembly
cytoplasmic translation
translation
mitochondrial respiratory chain complex assembly
NADH dehydrogenase complex assembly
ATP biosynthetic process
mRNA processing
RNA splicing
regulation of RNA splicing
circadian rhythm
cAMP–mediated signaling
nerve development
protein localization to extracellular region
response to hormone
entrainment of circadian clock
photoperiodism
regulation of glucocorticoid receptor signaling pathway
corticosteroid receptor signaling pathway
cytokine production involved in immune response
potassium ion transport
vesicle–mediated transport in synapse
ion homeostasis
sensory perception
regulation of neuron projection development
behavior
synapse organization
axonogenesis
chemotaxis
cell–cell adhesion
cognition
learning or memory
postsynapse organization
G protein–coupled receptor signaling pathway
synapse assembly
axon guidance
synaptic transmission, glutamatergic
regulation of postsynaptic membrane potential
protein localization to synapse
brain development
-log10(p.adj)

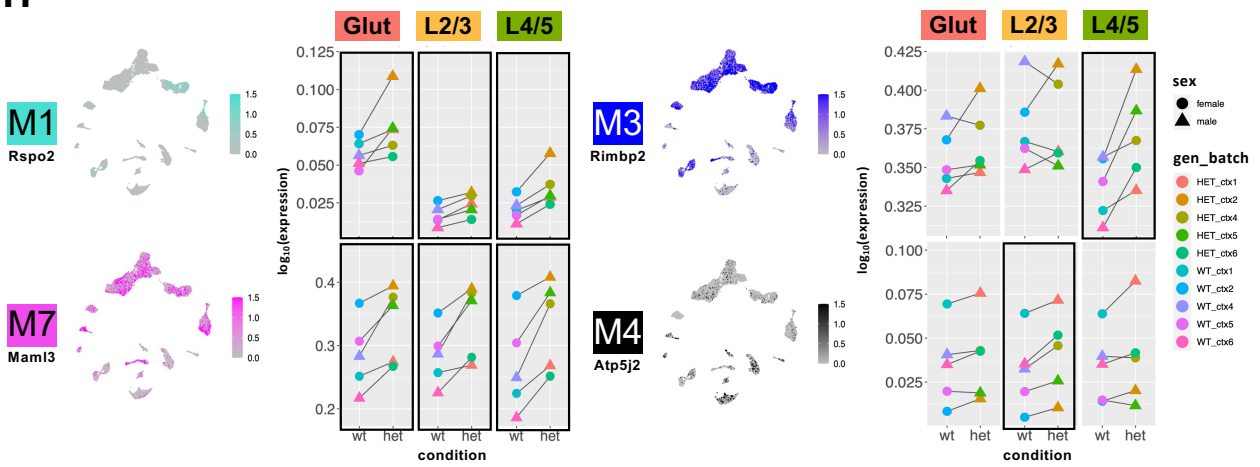
H
M1
Rspo2
M7
Maml3
M3
Rimbp2
M4
Atp5j2
Glut
L2/3
L4/5
log10(expression)
condition
wt
het
sex
female
male
gen_batch

228

Figure 3: hdWGCNA reveals differentially expressed glutamatergic cell coexpression modules. A) 10 glutamatergic modules identified via hdWGCNA B) Number of genes per module. C) Relative expression of glutamatergic modules across glutamatergic neuron subtypes (module score = average expression of all module genes compared to expression-matched background genes; DEMs identified via comparison of median pseudo-bulk logFC of module genes to that of the grey module via t-test; DEMs (*p < 0.05) in at least one population are labeled in yellow. D) DEG burden (calculated as in Fig. 2F) of each DEM in each cell type E) Heatmap of relative median pseudo-bulk logFC of module genes for glutamatergic cell types scaled by p-value. White and black boxes in C-E indicate the cell types in which each corresponding module was DE. F) Representative significant GO terms for Biological Processes enriched in glutamatergic modules. (*p < 0.05, **p < 0.01, ***p < 0.001). G) Box plots for 4 representative DEMs showing logFCs of module genes in each glutamatergic subtype. Non-opaque boxes indicate cell types where the module shown was significantly differentially expressed (P-value < 0.05). H) Feature plots (left) showing relative expression of representative genes from DEMs of interest in UMAP space. Dot plots (right) show median sample-level expression of the same genes. Black boxes indicate cell types where the corresponding module is differentially expressed, or where the direction of change in module expression is consistent across batches.

neurons (L6 CT and L6b), associated with general neuronal and synaptic functions. Although it includes both up- and downregulated genes, M1 shows a significant bias towards upregulation with the strongest effects in L4/5 IT and L5 IT subtypes. In contrast, M7 (featuring *Malm3*) is a smaller module exhibiting consistent upregulation across all glutamatergic subtypes. It is associated with general neuronal function as well as circadian rhythm and hormone response pathways. M3 (featuring *Rimbp2*) is selectively upregulated in more superficial glutamatergic subtypes L4/5 IT neurons, with enrichment for neuronal and synaptic processes. In contrast M4 (featuring *Atp5j2*) shows low expression across glutamatergic subtypes and GABAergic neurons, but relatively higher expression in non-neuronal cell types, with gene ontology terms related to translation and mitochondrial ATP metabolism. The shared dysregulation of M1 and M7 DEMs mirrors overlapping GO enrichment patterns across glutamatergic subtypes observed in GSEA (**Figure S2F**), supporting convergent molecular signature across glutamatergic neurons. The subtype-specific dysregulation of M3 and M4 suggest genotype-dependent perturbations of distinct biological processes particularly affecting L2/3 IT and L4/5 IT neuron populations.

Bulk RNA-seq comparison identifies shared signatures in constitutive versus conditional Chd8 mutants but divergent effects in nuclear versus synaptosomal mRNA fractions

261 We employed bulk RNA-seq as a complementary approach to snRNA-seq, assaying DE signatures
262 across four contrasts: mRNA from P60 cortex from constitutive *Chd8*$^{+/-}$ and from conditional *Camk2a-*
263 *Cre* x *Chd8*$^{+/flox}$ mice, and compartment-enriched nuclear and synaptosomal mRNA from P60 cortex
264 from *Chd8*$^{+/-}$ mice (**Figure 4**). See **Tables S9-S11** for sample details for each experiment, with N per
265 genotype group ranging from 6-16 samples with no obvious outliers and clear separation between
266 nuclear and synaptosomal fractions by PCA (**Figure S5A-C**). We used edgeR[62] including sequencing
267 batch and sex as covariates. We also analyzed male and female samples separately, finding generally
268 shared DE signatures (similar as for snRNA-seq) (**Figure S5D, Tables S12-15**). Across the four
269 conditions, the largest number of DEGs at either FDR < 0.1 or P < 0.05 was in the synaptosomal
270 preparation, followed by the nuclear preparation, then full cortex from *Chd8*$^{+/-}$ and lastly *Chd8*$^{+/flox}$
271 (**Figure 4A**). *Chd8* was among the top downregulated DEGs in all but the nuclear mRNA condition,
272 consistent with nonsense-mediated decay of mutant *Chd8* transcripts outside the nucleus (**Figure 4B**).
273 To identify shared and divergent DE signatures across conditions, we compared logFC of DEGs;
274 shared signatures are represented by concordant LogFC direction, condition-specific effects are
275 captured by patterns of change (up or down) in one condition with LogFC around zero in the other
276 condition, and divergent DE signatures are represented by opposite logFC direction. Comparison
277 between *Chd8*$^{+/-}$ and *Chd8*$^{+/flox}$ logFC for genes with FDR < 0.1 and P-value < 0.05 in *Chd8*$^{+/-}$ (**Figure**
278 **4C**) captured largely shared signatures, indicating that effects from post-mitotic heterozygous ablation
279 in excitatory neurons accounts for a significant part of DEG transcriptional pathology. DEGs identified in
280 both the nuclear and synaptosomal conditions (FDR < 0.1 and P < 0.05) showed strong concordance
281 with bulk cortex (**Figure 4D**), however there were striking differences and relatively low concordance
282 between nuclear and synaptosomal enriched mRNA fractions (**Figure 4E**).

283 To compare pathway-level dysregulation across bulk RNA conditions, we used GSEA to identify Gene
284 Ontology (GO) terms where the annotated gene set exhibited significant shift in LogFC distribution
285 towards up- or downregulation, with shared and condition-specific enrichment for representative terms
286 shown in **Figure 4F-G**. Most of the up- and down-regulated terms identified in the constitutive *Chd8*$^{+/-}$

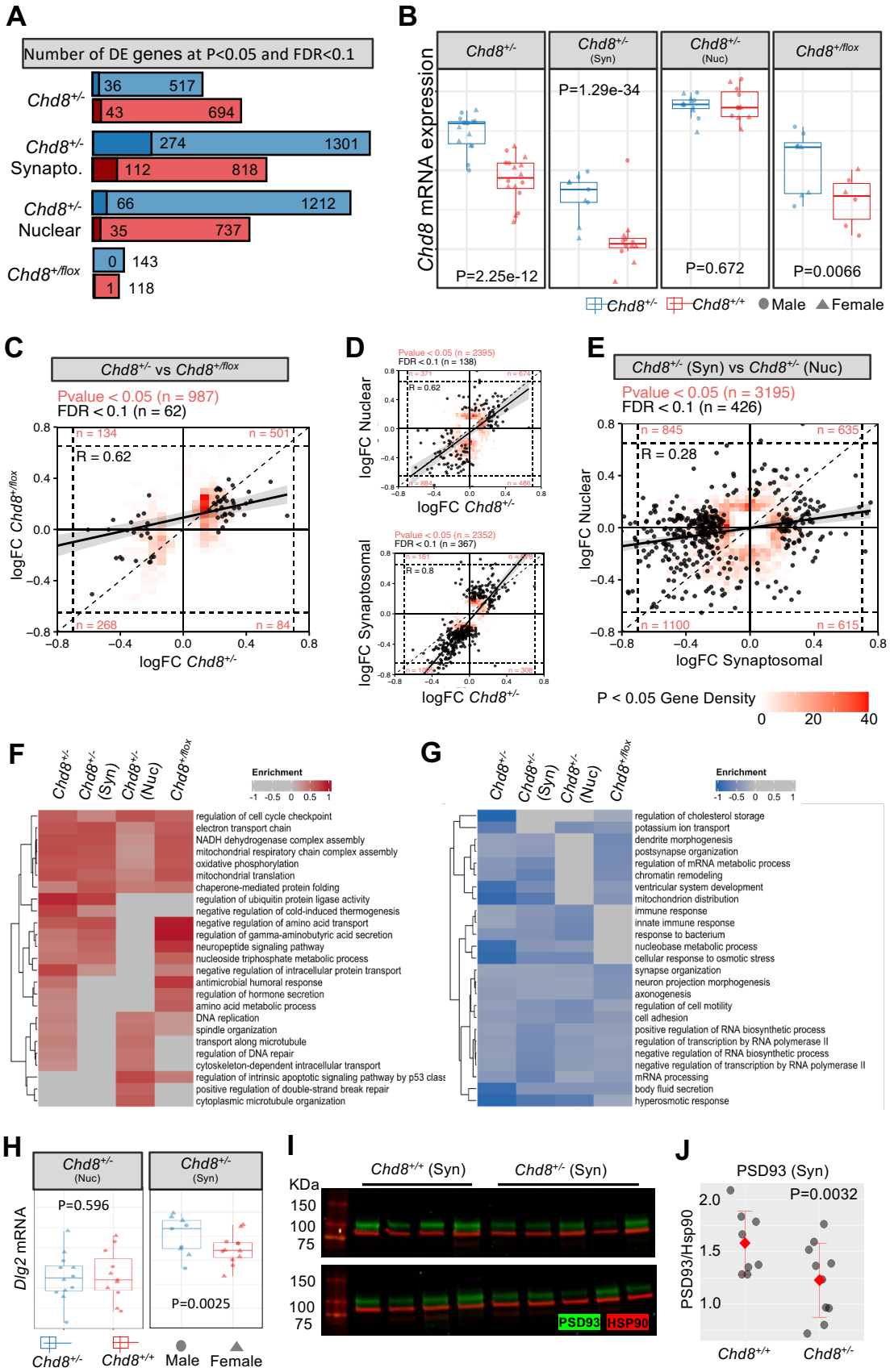
A
Number of DE genes at P<0.05 and FDR<0.1
Chd8+/-
36
517
43
694
Chd8+/- Synapto.
274
1301
112
818
Chd8+/- Nuclear
66
1212
35
737
Chd8+/flox
0
143
1
118
B
Chd8 mRNA expression
Chd8+/-
Chd8+/- (Syn)
Chd8+/- (Nuc)
Chd8+/flox
P=2.25e-12
P=1.29e-34
P=0.672
P=0.0066
Chd8+/-
Chd8+/+
Male
Female
C
Chd8+/- vs Chd8+/flox
Pvalue < 0.05 (n = 987)
FDR < 0.1 (n = 62)
n = 134
n = 501
R = 0.62
n = 268
n = 84
logFC Chd8+/flox
logFC Chd8+/-
D
Pvalue < 0.05 (n = 2395)
FDR < 0.1 (n = 138)
R = 0.62
logFC Nuclear
logFC Chd8+/-
Pvalue < 0.05 (n = 2352)
FDR < 0.1 (n = 367)
R = 0.8
logFC Synaptosomal
logFC Chd8+/-
E
Chd8+/- (Syn) vs Chd8+/- (Nuc)
Pvalue < 0.05 (n = 3195)
FDR < 0.1 (n = 426)
n = 845
n = 635
R = 0.28
n = 1100
n = 615
logFC Nuclear
logFC Synaptosomal
P < 0.05 Gene Density
0
20
40
F
Chd8+/-
Chd8+/- (Syn)
Chd8+/- (Nuc)
Chd8+/flox
Enrichment
-1 -0.5 0 0.5 1
regulation of cell cycle checkpoint
electron transport chain
NADH dehydrogenase complex assembly
mitochondrial respiratory chain complex assembly
oxidative phosphorylation
mitochondrial translation
chaperone-mediated protein folding
regulation of ubiquitin protein ligase activity
negative regulation of cold-induced thermogenesis
negative regulation of amino acid transport
regulation of gamma-aminobutyric acid secretion
neuropeptide signaling pathway
nucleoside triphosphate metabolic process
negative regulation of intracellular protein transport
antimicrobial humoral response
regulation of hormone secretion
amino acid metabolic process
DNA replication
spindle organization
transport along microtubule
regulation of DNA repair
cytoskeleton-dependent intracellular transport
regulation of intrinsic apoptotic signaling pathway by p53 class
positive regulation of double-strand break repair
cytoplasmic microtubule organization
G
Chd8+/-
Chd8+/- (Syn)
Chd8+/- (Nuc)
Chd8+/flox
Enrichment
-1 -0.5 0 0.5 1
regulation of cholesterol storage
potassium ion transport
dendrite morphogenesis
postsynapse organization
regulation of mRNA metabolic process
chromatin remodeling
ventricular system development
mitochondrion distribution
immune response
innate immune response
response to bacterium
nucleobase metabolic process
cellular response to osmotic stress
synapse organization
neuron projection morphogenesis
axonogenesis
regulation of cell motility
cell adhesion
positive regulation of RNA biosynthetic process
regulation of transcription by RNA polymerase II
negative regulation of RNA biosynthetic process
negative regulation of transcription by RNA polymerase II
mRNA processing
body fluid secretion
hyperosmotic response
H
Chd8+/- (Nuc)
Chd8+/- (Syn)
Dlg2 mRNA
P=0.596
P=0.0025
Chd8+/-
Chd8+/+
Male
Female
I
Chd8+/+ (Syn)
Chd8+/- (Syn)
KDa
150
100
75
150
100
75
PSD93
HSP90
J
PSD93 (Syn)
P=0.0032
PSD93/Hsp90
2.0
1.5
1.0
Chd8+/+
Chd8+/-

287

Figure 4: Shared DE in constitutive *Chd8*$^{+/-}$ and *Camk2a-CRE* conditional Chd8$^{+/flox}$ mice, with divergent impacts on nuclear and synaptosomal mRNA and protein. A) Barplot of DEG counts at P < 0.05 and FDR < 0.1 across bulk RNA-seq experiments (constitutive *Chd8*$^{+/-}$, *Camk2a-CRE* conditional *Chd8*$^{+/flox}$, and nuclear and synaptosomal preparations from the *Chd8*$^{+/-}$ line). B) *Chd8* mRNA is down-regulated in all but the nuclear preparation (P-values from EdgeR). C-E) Concordance plots comparing bulk RNA-seq logFC of DEGs detected in either dataset. Number of DEGs at different criteria listed above, R value for best fit line for FDR < 0.1 is listed on the plot. For P < 0.05, local density is plotted instead of individual data points due to large number of genes. For FDR < 0.1, individual datapoints are shown. The count of P < 0.05 DEGs in each quadrant listed in red. Higher data points in the upper right and lower left indicate logFC directional concordance between experiments. C) Concordance between constitutive and conditional datasets. D) Concordance for nuclear (top) and synaptosomal (bottom) versus whole cortex. E) Reduced concordance between nuclear and synapsomal datasets. F-G) Selected enriched GO terms for upregulated F) and downregulated G) genes across experiments. H) Downregulation of Dlg2 in synaptosomal RNA. I-J) Western blot (I) validating decreased synaptosomal PSD93 protein (J) in *Chd8*$^{+/-}$ cortex (N = 8 *Chd8*$^{+/+}$, 10 *Chd8*$^{+/-}$, P-value from Student's t-test).

were shared in the conditional *Chd8*$^{+/flox}$, and most terms in the nuclear or synaptosomal enriched conditions were shared in the full cortex preparation, findings that consistent with DEG concordance across contrasts above. We identified shared upregulation of terms including *Cell cycle checkpoint*, *Electron transport chain*, *Mitochondrial translation*, and *Chaperone mediated protein folding*, showing overlap with upregulatd gene modules and DEGs terms that were also detected in glutamatergic neuron subtypes in the snRNA-seq data (**Figure 3**). Among upregulated terms that differed between synaptosomal and nuclear conditions were *Regulation of gamma-aminobutyric acid secretion* and *Neuropeptide signaling pathway* in the synaptosomal and *Regulation of DNA repair* and *Transport along microtubule* in the nuclear fraction. For downregulated terms, *Axonogenesis*, *Synapse organization*, *Cell adhesion*, and *Regulation of transcription by RNA Pol II* were shared, while *Dendrite morphogenesis* and *Postsynapse organization* were example synaptosomal-enriched terms. Bulk RNA-seq results from the full cortex and from the nuclear and synaptosomal conditions showed evidence of correlation with DEG findings from snRNA-seq, though with substantial overall differences in DE signatures (**Figure S5E**). As expected, the nuclear enriched mRNA showed the highest correlation to snRNA-seq nuclear DE, as well as upregulation of genes associated with the glutamatergic M1 and M7 hdWGCNA modules that were broadly upregulated across glutamatergic subtypes in the snRNA-seq data, validating relevance of these broad DEMs (**Figure S5F**). GO terms associated with L2/3 IT

321 enriched upregulated M4 and M9 modules associated with mitochondrial energetics were among the
322 strongest bulk RNA-seq upregulated GSEA hits across conditions. We performed qPCR on 13 DE
323 targets from the constitutive cortex, all 13 genes tested showed the same direction of change as RNA-
324 seq DE analysis (**Figure S5G**). Finally, for the ASD and neuropsychiatric-associated synaptosomal-
325 specific downregulated *Dlg2* gene[63–66], which encodes the PSD93 excitatory synaptic scaffold protein,
326 we validated reduction at the protein level via Western blot (P = 0.0032, Student's t-test) in
327 synaptosomal preparations (**Figure 4F-4H**). These results solidify transcriptional pathology in adult
328 cortex due to *Chd8* haploinsufficiency, provide insights into cell-autonomous effects in post-mitotic
329 excitatory neurons, and suggest differential mRNA levels are driven by both transcriptional and post-
330 transcriptional mechanisms that have heightened impact on synaptosomal mRNA levels.

331 *Altered excitatory neuron spine dynamics and calcium signaling coherence in Chd8$^{+/-}$ mice*

332 The snRNA-seq and bulk RNA-seq both pointed to cortical excitatory neuron dysfunction and previous
333 studies have identified electrophysiological signatures in vivo and in vitro in glutamatergic
334 neurons[21,36,37,40,40,41]. To further investigate structural pathology of cortical neurons, we crossed *Chd8$^{+/-}$*
335 mice with thy1-YFP mice, which express cytoplasmic yellow fluorescent protein in a sparse subset of
336 layer 5 pyramidal neurons (L5 PyrNs)[67], and performed in vivo two-photon (2P) imaging on apical
337 dendrites of L5 PyrNs. We compared the density and dynamics of dendritic spines (postsynaptic
338 structure of majority excitatory synapse) between WT and *Chd8$^{+/-}$* littermates at adolescence (P30) and
339 adulthood (P90) mice (**Figure 5A**). Adolescent *Chd8$^{+/-}$* mice had lower spine density on the apical
340 dendritic tufts of L5 PyrNs (**Figure 5B**). Following the same dendritic segments over seven days, we
341 also found that *Chd8$^{+/-}$* mice had increased dendritic spine formation relative to WT mice, but
342 comparable spine elimination (**Figure 5C**). On the other side, adult *Chd8$^{+/-}$* mice had normal spine
343 density and dynamics (**Figure 5D-E**). These results indicate that *Chd8* haploinsufficiency delays
344 spinogenesis of cortical neurons during early development (before P30).

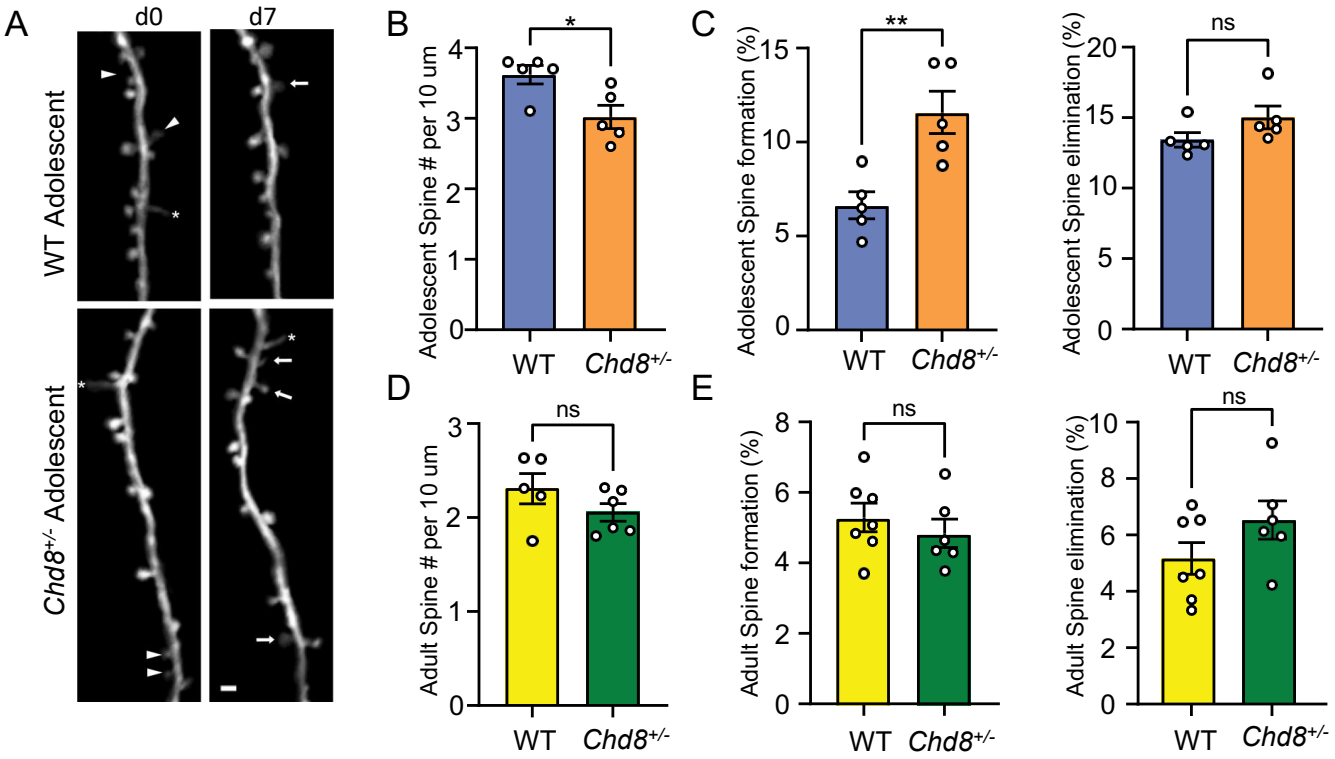

Figure 5: Delayed spinogenesis during *Chd8*$^{+/-}$ development. A) Dendritic segment imaged over 7-days in somatosensory cortex of adolescent WT and *Chd8*$^{+/-}$ mice. Arrowheads: eliminated spines; arrows: formed spines; asterisks: filopodia. Scale bar = 2 µm. B, D) Spine density in adolescent (b) and adult (D) *Chd8*$^{+/-}$ or WT littermates. C, E) The percentage of spines formed or eliminated over 7d is higher in adolescent (D) and adult (E) *Chd8*$^{+/-}$than WT littermates, mean, SEM., unpaired t-test. **p<0.01.

To understand how disruption of *Chd8* signaling affects the function of a cortical microcircuit, we performed calcium imaging in acute slices taken from wildtype or *Chd8*$^{+/-}$ mouse brains expressing the genetically encoded calcium indicator *GCamp6f* in prefrontal cortex neurons under the control of the human *Synapsin* promoter (**Figure 6A-D**). We collected 60-minute recordings from a total of 544 neurons from 8 wildtype slices (68+/-9 neurons/slice) and 818 neurons from 10 *Chd8*$^{+/-}$ slices (82+/-9 neurons/slice). Overall, the activity of wildtype and *Chd8*$^{+/-}$ slices was similar (**Figure 6E-F**; mean fraction of frames active = 5.2+/-0.2% WT vs 5.0+/-0.2% HET, p = 0.4, t-test). To examine the functional connectivity across the prefrontal microcircuit, we binned neurons into eight 75 µm bins starting at the cortical surface and extending to a depth of 600 µm, and calculated the correlation coefficient between the activity of neurons according to the location of each neurons within the slice, then averaged the correlation coefficient based on the depth of 600 µm, and calculated the correlation

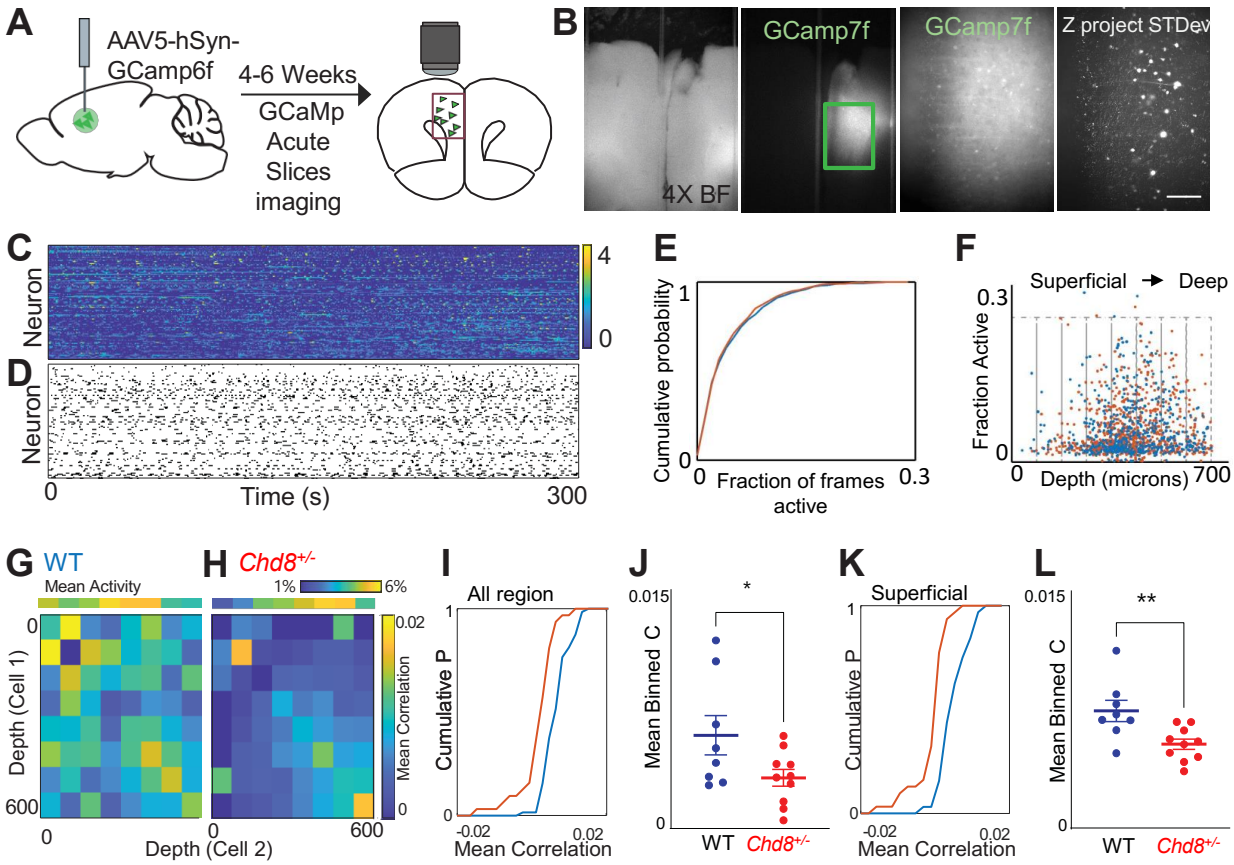

Figure 6: Disruption of coordinated activity in *Chd8*$^{+/-}$ PFC microcircuits. A. Mice injected with *Syn-GCamp6f* and activity recorded from acute slices after 4-6 weeks. B, wide field and GFP at 4x (left). 10X of individual neurons and z-projection of standard deviation across frames (right). C, z-scored fluorescence traces from neurons in a single slice. D, Raster of events. E, Cumulative probability function showing overlap in fraction of frames active for neurons from WT (blue) and *Chd8*$^{+/-}$ (red) slices. F, Activity of each cell as a function of depth from cortical surface. Cells binned by distance from surface (gray boxes) and mean correlations within and between bins calculated. G, H, 8x8 matrix of mean correlation coefficient calculated for cells within each pair of bins, averaged for WT (G) or *Chd8*$^{+/-}$ (H) slices. I, cumulative distribution function (CDF) of mean correlation across 544 pooled WT (blue) neurons and 818 pooled *Chd8*$^{+/-}$ (red) neurons for all bins. J, Mean correlation coefficient of WT and *Chd8*$^{+/-}$ slices ($p < 0.05$, t-test). K, CDF of the mean value of the subset of bins in which neuron 1 was < 300 microns from cortical surface. L, Mean correlation coefficient of superficial neurons in WT and HET slices ($p < 0.01$, t-test).

coefficient between the activity of neurons according to the location of each neurons within the slice, then averaged the correlation coefficient based on the position of each neuron in the cell pair (**Figure 6G-H**). Visual examination of the resulting matrix of averaged correlations revealed that neuron pairs from heterozygous *Chd8*$^{+/-}$ slices had on average lower correlation coefficients compared to neuron pairs from WT slices, and this was particularly pronounced when at least one neuron was located in the

381 superficial (< 300 μm from the cortical surface) aspect of the slice (**Figure 6I-L**; mean correlation
382 coefficient WT 0.0057 +/-0.0001 vs 0.0030+/-0.0005, $p < 0.05$, t-test; n = 8 WT and 10 HET slices;
383 mean correlation coefficient superficial WT 0.0050+/-0.0009 vs HET 0.0021+/-0.0004, $p < 0.01$, t-test; n
384 = 8 WT and 10 HET slices), suggesting that these neurons are relatively disconnected from deeper
385 layer neurons in the prefrontal microcircuit of mutant *Chd8*$^{+/-}$ animals.

386 *Chd8*$^{+/-}$ *mice exhibit disrupted sleep*

387 Sleep issues are a common symptom in humans with *CHD8* mutations and the transcriptional
388 dysregulation in *Chd8*$^{+/-}$ mice featured upregulation of the circadian-associated M7 glutamatergic
389 module. Thus, we used EEG/EMG to continuously record neural activity during a 24-hour period,
390 assigning states of REM, NREM, and Wake, analyzing 11 *Chd8*$^{+/-}$ (female=7, male=4) and 8 WT
391 littermates (female=4, male=4) (**Figure 7A-B'**). The total time in seconds that each mouse spent in
392 each state was calculated for each hour (**Figure 7C-D**). For comparison of sleep patterns, total and
393 standard deviation (SD) were calculated by subject using hourly values and compared for light
394 (Zeitgeber Time ZT0-ZT12) and dark (ZT12-ZT24) phases (**Figure 7E-F**). *Chd8*$^{+/-}$ mice had a significant
395 increase in time spent in REM in the dark stage (P = 0.036, unpaired t-test with Welch's correction),
396 and significantly less time spent in NREM (P = 0.008, unpaired t-test with Welch's correction) and
397 increased time spent in wake state (P = 0.040, unpaired t-test with Welch's correction) in the light
398 phase. Comparing SD of the time spent per state across hours, *Chd8*$^{+/-}$ mice showed higher variability
399 in all states. SD of REM time was significantly higher during both light and dark phases (P = 0.012 and
400 0.003, respectively), and SD of NREM and Wake time were significantly higher during dark phase (P-
401 values = 0.017 and 0.006, respectively) and marginally increased during the light phase (P = 0.115 and
402 0.059 respectively). Together results revealed disrupted sleep patterns in *Chd8*$^{+/-}$ mice, including more
403 time in REM and time spent in Wake in the light stage, and higher variability in time spent in specific
404 sleep/wake states across the light and dark stages.

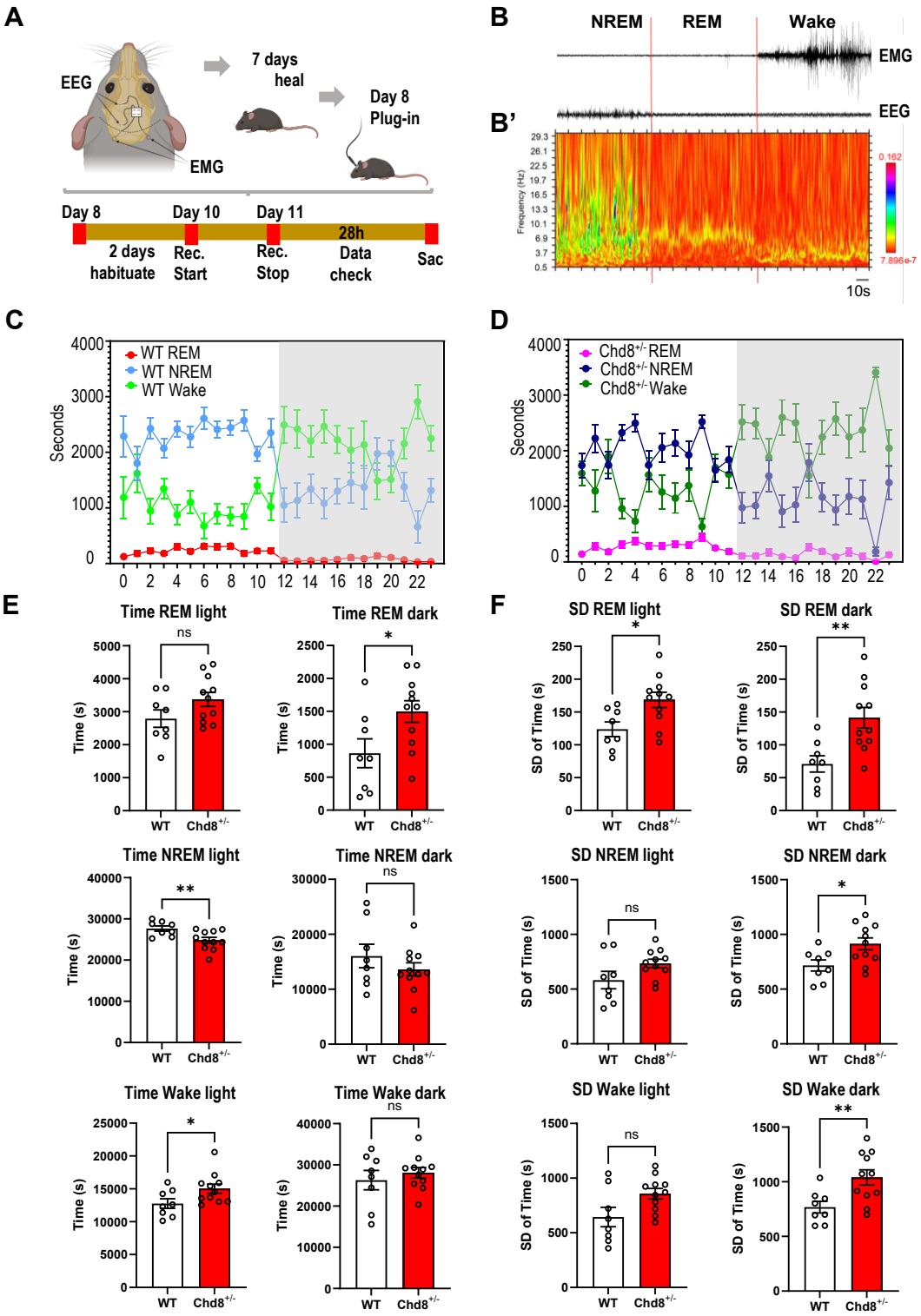

Figure 7: Perturbed sleep patterns in *Chd8*$^{+/-}$ mice. A) Schematic of 24hr EEG/EMG sleep analysis. B) Example EEG/EMG traces showing activity during REM, NREM, and Wake state. B') Spectrogram of the EEG signal in B C-D) Summary of time spent in each state during each hour of the 24hr monitoring period for wild type (C) and *Chd8*$^{+/-}$ (D) groups. E) Summary of mean total time spent in each state separated by light and dark stages. F) Summary of SD of time spent in each state. Mean and SD shown, significance form unpaired t-test with Welch's correction. See text for details.

412 **Discussion**

413 This study extends understanding of how *Chd8* haploinsufficiency alters the adult mouse cerebral
414 cortex across transcriptomic and functional modalities. Via stereology and snRNA-seq, we show that
415 increased cortical volume in *Chd8*$^{+/-}$ mice is not due to increase in cortical excitatory neuron numbers,
416 and, in fact, is associated instead with decreased neuron density. While macrocephaly was not due to
417 increased numbers in excitatory neurons, these cells do exhibit sensitivity to *Chd8* haploinsufficiency at
418 the level of cell-type specific transcriptional pathology, synaptosomal RNA homeostasis, dendritic spine
419 formation, and signaling coherence. Finally, we expand the phenotypic testing of heterozygous *Chd8*
420 mouse models in the domain of sleep, finding perturbations to sleep state that aligns with high
421 prevalence of sleep disturbance reported in patients carrying *CHD8* mutations. Overall, our findings add
422 to the understanding of the effects of heterozygous *Chd8* mutation on the mouse cortex, providing new
423 insights into anatomical, cellular, and circuit impacts, dosage sensitivity during brain development and
424 in post-natal postmitotic neurons, and demonstrating presence of sleep disturbance.

425 Increased brain size during development and increased cortical volume in adult mice has been reported
426 across different mutant *Chd8* mouse lines[20,25,27,29]. *Chd8* haploinsufficiency has also been linked to
427 altered neurogenesis in mouse[20,25,28] and in vitro in human cellular and organoid brain models[32,38].
428 While increased production of cortical excitatory neurons during development leading to increased
429 neurons in the adult cortex seemed a plausible explanation for cortical volume increase, results from
430 both stereology and snRNA-seq show this to not be the case in *Chd8*$^{+/5bpdel}$ mice. In fact, we found the
431 opposite pattern of decreased excitatory neuron density driven by increased volume without increased
432 neuron counts or increased soma size. There was a trend of decrease in proportions of certain
433 glutamatergic types in snRNA-seq data, reaching significance for decreased in L6 IT neurons in the
434 mutants. snRNA-seq indicated significant increase in proportion of OPCs and trend towards increase in
435 astrocytes, raising the possibility that increased proportions of non-neuronal cells may explain some of
436 the increased cortical volume. Whatever the roots of *Chd8*-associated macrocephaly, it is unclear what
437 the link between this neuroanatomical signature and relevant social and cognitive phenotypes, with a

438 recent study finding little correlation between adult brain weight and behavioral phenotypes for *Chd8*$^{+/-}$
439 mice from a series of genetic backgrounds[34]. It could be that causes of macrocephaly and behavioral
440 phenotypes in *Chd8*$^{+/-}$ mice are independent, or that the mechanisms for are linked, but with variable
441 anatomical and behavioral outcomes in adult mice. Our results do point to glutamatergic pathology and
442 one intriguing possibility is that changes in neuronal morphology and microstructure organization, for
443 example dendritic arborization, could account for the changes. Further studies will be needed to resolve
444 specific causes of volume increase in *Chd8*$^{+/-}$ adult cortex.

445 Via unbiased snRNA-seq, we found that glutamatergic neurons exhibit the strongest transcriptional
446 pathology across cell types in adult mouse *Chd8*$^{+/-}$ cortex, with the most extensive impacts in L2/3 IT
447 and L4/5 IT subtypes. We identified subtype-specific and shared glutamatergic DEMs, including shared
448 upregulation of M1 and M7 modules, which are associated with general neuron-associated pathways
449 and with specific circadian rhythm GO terms. Transcriptional pathology in bulk RNA-seq analysis of
450 constitutive and conditional *Chd8*$^{+/-}$ mutants here aligns with *CHD8* studies in vitro and using mouse
451 models[12,20,22,24,25,28,68], with our study adding substantially via integrating single cell and bulk, constitutive
452 and conditional mouse models, and synaptosomal mRNA fractions. These findings include upregulated
453 aerobic respiration and mitochondrial energetics, which we map to having the strongest signature in
454 L2/3 IT neurons, and downregulation associated with synaptic organization and signaling. Bulk RNA-
455 seq transcriptional changes in excitatory neuron-specific *Chd8*$^{+/flox}$ mice paralleled changes in
456 constitutive heterozygous *Chd8*$^{+/-}$ mutants, demonstrating continued requirement for full *Chd8* dosage
457 and indicating that the majority of excitatory neuron transcriptional phenotypes in mature *Chd8*$^{+/-}$ mice
458 may be independent of developmental impacts. Our findings of effects in *Chd8*$^{+/flox}$ mice due to ablation
459 in excitatory neurons are consistent with effects reported in earlier in vitro studies of both heterozygous
460 and homozygous neuronal ablation[40,69], and extend previous studies of adult homozygous mutant
461 *Chd8*$^{-/-}$ conditional mutant mice that did not examine NDD-relevant heterozygous mutants[44]. We further
462 link transcriptional dysregulation in glutamatergic neurons to functional impacts in these cells, finding
463 altered dendrite spine formation during adolescence which manifests at the circuit level as de-

464 correlated spontaneous prefrontal activity. Finally, though not directly linked to specific cells or circuits,
465 we identified perturbed sleep patterns *Chd8*$^{+/-}$. These findings are highly relevant to NDDs, as disrupted
466 synaptic development and altered network activity represent candidate causal mechanisms and sleep
467 disturbances are commonly reported in individuals with ASD and related conditions[70] and are one of the
468 more penetrant phenotypes in CHD8-NDD[71]. We previously tested *Chd8*$^{+/5bpdel}$ mice across a battery of
469 behavioral assays, finding deficits in novel object recognition and fear conditioning in the learning and
470 memory domain with no differences in sociability using the three-chamber social preference test or in
471 male-female interactions[20]. Other constitutive *Chd8*$^{+/-}$ mouse studies similarly have not identified classic
472 sociability deficits in the three-chamber social preference assay and behavioral and cognitive
473 phenotypes vary across *Chd8*$^{+/-}$ studies and across mouse genetic backgrounds[20–22,24,25,27,34,37]. As
474 such, behavioral studies of *Chd8* mutant mice have proved challenging to interpret. Our results, along
475 with studies that have identified other phenotypes at cellular, molecular, and anatomical level such as
476 via electrophysiology or structural MRI, highlight molecular endophenotypes that may be more
477 consistent in expression and have high translational relevance. Future studies will be needed to
478 determine which aspects of *Chd8*$^{+/-}$ mouse phenotypes are driven by developmental versus later
479 requirement for full dosage, which specific neuronal and glial populations are dependent on *Chd8*, and
480 if molecular, cellular, and neuroanatomical phenotypes are consistent between mutant lines and across
481 mouse and human *CHD8*$^{+/-}$ models.

482 One novel finding from our study was the significant differences in DE signatures between nuclear and
483 synaptosomal mRNA preparations. Bulk nuclear RNA-seq recapitulated upregulation observed for the
484 two glutamatergic DEMs with broad dysregulation and had the highest concordance with snRNA-seq
485 DEGs, as well as being strongly concordant with the full bulk cortex RNA-seq. Thus, nuclear RNA
486 changes observed at both single cell/nucleus and bulk level appear robust. Surprisingly, there was
487 relatively weak concordance between synaptosomal and nuclear DEGs, with a stronger overall DE
488 signature in the synaptosomal enriched preparations. These findings indicate disconnect between
489 changes in transcriptional rate, captured by nuclear RNA datasets, and changes in steady-state mRNA

490 levels at the synapse in *Chd8*$^{+/-}$ cortex. We and others previously identified altered mRNA splicing in
491 *Chd8*$^{+/-}$ mouse and *in- vitro* models[20,72], raising the possibility that *Chd8* haploinsufficiency directly or
492 indirectly alters RNA processing. ChIP-seq studies of CHD8 have consistently identified enrichment of
493 regulatory targets associated transcription and RNA processing[73]. We did observe down-regulation of
494 RNA processing associated with L4/5 IT specific DEM M6, though this was specific to this population.
495 Beyond a better understanding of the molecular function of Chd8, future studies are needed to
496 determine whether the synaptosomal DEG signature is specific to synaptosomal localized mRNA, or a
497 more broadly present in cytosolic mRNA overall, what the cell-type specific impacts are on mRNA
498 processing and localization, whether synaptosomal RNA differences are associated with differences in
499 synaptic protein makeup and synaptic function, and if this finding extends to *CHD8*$^{+/-}$ human neurons.
500 Of more broad relevance, our findings of altered post-transcriptional RNA dynamics link CHD8 with
501 other ASD/NDD genes with primary function in RNA processing, for example *FMR1*/FMRP[74,75], and our
502 finding of pathology arising do to disruption of this function may by a more broad hallmark of ASD[76,77].

503 There are limitations to this work that should be considered. The number of replicates (N=5 per
504 genotype) was cost-limited for snRNA-seq, somewhat limiting statistical power. Additionally, nuclei-
505 based methods may miss changes in cytosolic mRNA levels[78,79], which may be relevant based on our
506 bulk analysis. Further, there are challenges with snRNA-seq for DE testing at single gene level using
507 individual cells/nuclei. While Wilcoxon tests are commonly used in single cell differential expression
508 analysis, we found this method yielded high false positive rates (as issue that has been raised
509 previously[80]). In contrast, pseudobulk and hdWGCNA methods take advantage of aggregating cells or
510 genes to compare expression at the cluster or module level, giving more robust DE results at the cost
511 of reducing resolution for single cell and single gene level effects. Finally, it is unclear how much the
512 transcriptomic pathology extends to protein level or impacts function. With regard to functional studies,
513 we chose three *in vivo* assays to focus on: spine dynamics, correlated GCaMP signaling, and sleep.
514 Previous studies have not tested these phenotypes, and we believe our results provide new insights
515 into pathology. However, other assays would be valuable and each of the domains we studied could be

516 investigated at higher depth. We did not test conditional *Chd8*$^{+/flox}$ mice beyond bulk RNA-seq, leaving
517 unanswered whether this model recapitulates other pathology. Finally, *Chd8* mutant mouse lines exhibit
518 variation in phenotype penetrance and expressivity, which is at least in part due to the impact of genetic
519 background[34]. Considering this, our findings may not be conserved in other *Chd8* mouse models,
520 though we note overlapping transcriptional signatures described here and in other studies as
521 summarized above. While these limitations hold, our results lay the foundation for future work
522 characterizing constitutive and conditional mutant *Chd8* mouse models.

523 In summary, our study extends understanding of the impacts of *Chd8* haploinsufficiency in vivo in
524 mouse brain, with a focus on glutamatergic excitatory neurons. We show that constitutive and
525 conditional heterozygous ablation leads to convergent transcriptional pathology and to impacts on
526 neuronal spinogenesis and circuit function. Our findings illustrate how loss of *Chd8*, which has received
527 attention for high expression in early development and role as a chromatin remodeler, impacts the cell-
528 type specific makeup and pathology of the adult cortex and impacts post-transcriptional mRNA
529 dynamics, extending understanding across molecular, cellular, circuit, and organismal phenotypes. Our
530 findings support a framework where excitatory neuron dysfunction at the level of cortical excitatory
531 synapses and circuits may be an area of casual convergence in NDDs and raising the possibility that
532 interventions targeting postnatal postmitotic cortical neurons may be effective at addressing at least
533 some of the underlying NDD pathology.

Acknowledgements

This work was supported by the National Institutes of Health National Institute of Mental Health (NIH NIMH) R01 MH120513 to A.S.N., National Institute of Neurological Disorders and Stroke (K08 NS105938-01A1 to N.A.F.), the Simons Foundation (Award # 604325) and the National Institute of Mental Health (R01MH117961 to V.S.), as well as the UCSF Dolby Family Center for Mood Disorders. C.P.C. was supported by the NIH NIMH Autism Research Training Program fellowship (T32 MH073124-16). S.L. was supported by T32 GM 007377 and F31 HD113328-01A1. A.A.W. was supported by NIH NIMH F31 MH119789 and T32 GM007377. We thank Dr. Wenjie Bian and Dr. Luis de Lecea at Stanford University, for their technical advice on EEG/EMG experiments and data analysis. We thank Dr. Caitlin Moyer for her technical assistance and for contributing to the execution of the spine imaging analysis.

Author contributions

A.S.N. conceived the project with substantial contributions from Y.Z., D.A. and V.S. C.P.C. led the project execution, designed experimental work and oversaw most aspects of data generation and analysis. S.A.L. fully executed snRNA-seq bioinformatics and led most of the data analysis with contributions from K.C., N.S., E.F., N.C., E.S., C.A., A.W. and A.S.N. C.P.C., W.A., J.B., and S.F. carried out experimental stereology and analysis. C.P.C., S.A.L., P.B., A.K.S., D.P., D.R., S.M., M.C., L.D., J.Z. and R.O. carried out experiments. C.M. and J.B. performed 2P spine imaging and analysis, J.S., B.M., and J.L. performed EEG recording and analysis. C.P.C., S.A.L. and A.S.N. wrote the manuscript.

557 **Methods**

558 **Animals**

559 Generation of Cas9-mediated 5bp frameshift deletion in exon 5 of *Chd8* in mice (here referred to as
560 *Chd8*$^{+/-}$ mice) was previously described[20]. For in vivo imaging, this mouse line was crossed with the
561 thy1-YFP-H (JAX strain: 003782) mouse line and maintained in the C57BL6/J (JAX strain: 000664)
562 background. Mutant mice *Camk2a-CRE Chd8*$^{+/flox}$ were obtained by crossing Chd8 loxP mice on
563 C57BL/6J (*Chd8*^{em3Lutzy}; JAX strain: 031555) to Camk2a-CRE (*B6.Cg-Tg(Camk2a-cre)T29-1Stl/J*; JAX
564 strain: 005359) to achieve heterozygous ablation in post-mitotic forebrain glutamatergic neurons. All
565 protocols utilized in the generation of mouse brain samples were approved by the Institutional Animal
566 Care and Use Committees (IACUC) at the University of California Davis and University of California
567 Santa Cruz. Mice were housed in a temperature-controlled vivarium maintained on a 12-h light–dark
568 cycle. We made efforts to minimize pain, distress and the number of animals used in the study.

569

570 **Histological tissue preparation and Nissl Stain**

571 Thirty-six 42-day-old mice were included in this analysis (16 brains per genotype, 16 per sex).
572 Mice were anesthetized using Isoflurane and perfused transcardially using room temperature saline
573 solution (0.9% NaCl) followed by 4% paraformaldehyde (PFA) in 0.1 M phosphate buffered (PB) saline
574 using a peristaltic pump (Minipuls 3, Gilson) at 20 rpm flow rate. Brains were removed and post-fixed in
575 4% PFA at 4ºC for 24 h. Fixed brains were cryoprotected in 50 ml of 10% and 20% glycerol solutions
576 with 2% DMSO in 0.1 M phosphate buffer (PB; pH 7.4; for 24 and 72 hours, respectively). Brains were
577 blocked at -2.00mm posterior to the interaural line prior to flash freezing. Sections were cut using a
578 freezing, sliding microtome in 4 series at 60 µm (Microm HM 440E, Microm International, Germany).
579 Every 4th section was collected in 10% formaldehyde in 0.1 M PB (pH 7.4) and post-fixed at 4ºC for 1
580 week[81]. Sections were rinsed twice for 1 hour each in 1ml of 0.1M PB, mounted on gelatin-coated
581 slides, and air-dried overnight at 37°C. Defatting was performed in a mixture of chloroform/ethanol (1:1,
582 vol) for 2 x 1 hour. The brains were rehydrated in graded alcohols; 100% ethanol, 100% ethanol, 95%

583 ethanol, 70%, 50% and dipped in deionized water[81,82]. Sections were stained 40 seconds in a 0.25%
584 thionin solution (Fisher Scientific, Waltham, MA, cat. no. T-409), dehydrated through graded alcohols,
585 differentiated in 95% ethanol and 5 drops of glacial acetic acid, cleared in xylene and cover-slipped with
586 DPX (BDH Laboratories, Poole, UK)[81].
587

588 **Stereology**

589 The inferior boundary of the cortex was defined as the bottom of the agranular insular area (AIA), and
590 the superior boundary was defined as the anterior cingulate area (ACA) or the retrosplenial area (RSA)
591 and the white matter was then followed to the ACA/RSA border[83]. Neuron number, neuronal soma size,
592 and brain volume were estimated using Stereoinvestigator V10.50 (MBF Biosciences, Williston, VT)
593 attached to a Zeiss Imager.Z2 Vario with a Zeiss AxioCam MRc. An EC PlanNeoFluar 2.5 x objective
594 was used to trace the outline of the cortex and a PlanApoChromat 100x oil objective was used for cell
595 counts and soma size determinations. The volume of the cortex was determined using the Cavalieri
596 method[53,54,84]. For each mouse, 15-18 sections (480 μm apart) were analyzed with the first section
597 chosen randomly amongst the first through the cortex. Estimates of neuron numbers were obtained
598 using the Optical Fractionator method[55,85]. Since no lateralization was found in the volumetric estimates
599 ($p = 0.65$), we sampled the left hemisphere of half of the mice and the right hemisphere of the other half
600 for estimates of neuron numbers. We used the same sections that were used for volumetric estimates.
601 We used a counting frame size of 18x18x10μm with 2 μm guard zones, and a scan grid of 480x480 μm
602 placed at a random angle. Neurons were defined following established protocols[53–55,84–86] based on: 1)
603 dark staining, 2) a well-defined nucleolus and 3) a round, non-jagged cell body[81,86–89]. Section thickness
604 was measured at every counting site. The volume of neuronal somas was determined using the
605 Nucleator method[90] during the Optical Fractionator analysis. Comparison of stereological measures
606 (volume, neuron number, and soma size) were performed via ANOVA to examine global effects of sex
607 and genotype and test for sex by genotype interaction, and then via t-test to compare the effect of
608 genotype in males and females. In addition to test results, effect sizes are reported for ANOVA (partial

609 eta squared, η_p^2) and t-test (Cohen's d). Statistical analyses were performed using SPSS (version 26),
610 plots were generated using *ggplots2* package in R programming language[91].
611
612 **Rostro-Caudal Volume analysis.**
613 To investigate the effects of genotype and sex on Cavalieri counts, mixed-effects regression models
614 were employed using the `lme4` and `lmerTest` packages in R. The initial model tested the main effect
615 of genotype on Cavalieri counts while accounting for sex, batch effects, and the z-position of the mouse
616 brain sections. Polynomial terms up to the fourth degree for z-position (Zpos) were included to capture
617 potential non-linear relationships observed in exploratory data analysis. Subsequently, a model was
618 fitted to examine the interaction between genotype and sex, including an interaction term for these
619 variables. This model was structured to evaluate whether the effect of genotype on Cavalieri counts
620 varied by sex. The analysis was extended to assess the effects of genotype across different rostral-
621 caudal brain segments. The segments - Rostral, Median, and Caudal - were defined based on changes
622 in direction observed in the z-position plot, aiming to reflect the anatomical structure of the mouse brain.
623 Dummy coding was applied to compare each segment against the reference levels. The final model
624 included these segments as factors, alongside the previously mentioned covariates and polynomial
625 terms for z-position. For data visualization, the `ggplot2` package was utilized to create plots depicting
626 the relationship between z-position and Cavalieri counts. Separate smoothed plot lines were generated
627 for each sex and genotype combination, providing a clear visual representation of the data across
628 different brain regions. All statistical analyses were performed using R. The mixed-effects models
629 allowed for robust estimation of fixed effects while accounting for random effects associated with batch
630 and individual mouse variations.
631
632 **Adult mouse cortex dissections**
633 Mice were anesthetized with isoflurane and euthanized via cervical dislocation in accordance with
634 institutional animal care protocols. Brains were rapidly extracted, and cerebral cortices were dissected
635 on ice following standard anatomical landmarks. Dissected tissues were snap-frozen in liquid nitrogen

636 or dry ice to preserve molecular integrity and minimize RNA degradation, and stored at -80°C until
637 further use. These samples were subsequently used for RNA extraction, nuclear isolation, or cellular
638 fractionation, as described below.
639

640 **Cellular Fractionation (synaptosomal preparation)**

641 Brains from *Chd8*$^{+/-}$ and wild-type littermates were collected on or around PND60. Following cervical
642 dislocation, brains were sub-dissected to isolate Cortex. Flash frozen cortices were stored at -80C until
643 further processing. On the day of cellular fractionation, samples were treated with Syn-Per reagent
644 (ThermoFisher Scientific Catalog #87793) to obtain cytosol, synaptosome and flowthrough ("total")
645 fractions. The "total" fraction was then used treated with "NE-PER™ Nuclear and Cytoplasmic
646 Extraction Reagents" (cat #78833) to obtain the nuclear, and a "cleaner cytosol" fractions. Total RNA
647 from these fractions was then extracted using RNA RNAqueous™ Total RNA Isolation Kit (cat#
648 AM1912 ThermoFisher Scientifics). Manufacturer protocols were followed with minor adjustments to
649 increase RNA yield from cellular fractions. Adjustments included combining the cortex samples with
650 500µl of Syn-Per reagent and 5µl of protease inhibitors during homogenization, based on our starting
651 sample amount, and adding 350µl of RNA extraction lysis buffer immediately after fractionation to the
652 synaptosome and nuclear fractions.
653

654 **RNA Isolation, bulk RNA-Sequencing and bioinformatics analysis**

655 Mouse cortices were collected at around PND60 from the following groups: 15 wild-type (WT) mice and
656 16 *Chd8*$^{+/-}$ mice (8 males and 7 females in the WT group; 7 males and 9 females in the *Chd8*$^{+/-}$ group),
657 as well as 8 WT and 6 *Chd8*$^{+/flox}$ mice (5 males and 3 females in the WT group; 4 males and 2 females
658 in the *Chd8*$^{+/flox}$ group). Samples were snap frozen on dry ice and stored at -80C until RNA preparation.
659 Total RNA was obtained using RNAqueous Total RNA Isolation Kit (cat# AM1912 ThermoFisher
660 Scientifics), and assayed via Agilent RNA 6000 Nano Bioanalyzer kit/instrument. Sample RIN scores
661 ranged from 8 to 9.4. Poly-A-enriched mRNA libraries were prepared at Novogene using Illumina
662 reagents. Libraries were sequenced using Illumina NovaSeq 6000 S4 system, paired-end 150 (PE150)

method. Reads were aligned to mouse genome (GRCm38/mm10) using STAR (version 2.5.4b)[92], and gene counts were produced using featureCounts[93]. On average, 50 million paired-end reads (PE) aligned per sample, with a range of 32 to 84 million reads. Data quality was assessed using FastQC[94], and principal component analysis (PCA) was used to determine presence of sample outliers. All 24 samples were qualified for the analysis. Raw RNA-seq fastq files and a gene count matrix is available on GEO (GSE300997). Bioinformatic analysis was performed using R programming language version 4.2.1 (R Development Core Team, 2015) and RStudio integrated development environment version 2023.06.0 (Team R, 2018). Plots were generated using ggplot2 R package version 3.4.0. Heatmaps were generated using pheatmap R package 1.0.12. In addition to total cortical RNA-seq, bulk RNA-sequencing was also performed on nuclear and synaptic fractions isolated from the cortex of *Chd8*$^{+/-}$ (germline heterozygous) and wild-type littermates at PND60. A total of 13 *Chd8*$^{+/-}$ and 12 wild-type nuclear fraction libraries were sequenced from both male and female mice. Following quality control (**Figure S5C**), 9 mutant (4 male, 5 female) and 12 wild-type (7 male, 5 female) nuclear libraries were retained for downstream analysis. For the synaptic fraction, 11 wild-type (6 male, 5 female) and 9 mutant (3 male, 4 female) libraries were sequenced, of which 7 mutant and 11 wild-type libraries passed QC and were used for downstream analysis. RNA from both fractions was processed using the same RNA isolation and sequencing protocols as described above. Raw and processed data for these samples are also available through GEO (GSE300997).

Bulk differential expression (DE) analysis

For DE analysis we used edgeR R package[62]. Genes with a minimum of 1 counts per million (CPM) in at least six samples were included in the analysis. The first surrogate variable from the SVA-batch-correction method was used as a covariate in the edgeR GLM model[95]. For sex-stratified DE, we used a threshold of CPM > 1 in at least 3 samples, and no batch correction. Reads Per Kilobase per Million mapped reads (RPKM) were used for plotting summary heatmaps and expression data of individual genes.

690 **Bulk gene ontology enrichment analysis**

691 To test for enrichment of GO terms we used the TopGO R package version 2.34[71]. Mouse Gene
692 Ontology (GO) data was downloaded from Bioconductor (org.Mm.eg.db). For the analysis presented
693 here, we restricted our testing to GO Biological Process annotations and required a minimal node size
694 of 20, and at least 2 significantly DE genes in a GO term. We used the internal 'weight01' testing
695 framework and the Fisher exact test, a strategy recommended for gene set analysis that generally
696 accounts for multiple testing comparisons. For GO BP analysis, we reported terms with p-value<0.05.
697 For all enrichment analysis, the test set of DE genes was compared against the background set of
698 genes expressed in our study based on minimum read-count cutoffs described above.

699

700 **Quantititavice PCR (qPCR) target validation**

701 qPCR was performed using the Analytik Jena qTower³ thermal cycler and PowerSYBR reagent
702 (Thermo Fisher Scientific), following the manufacturer's protocols. Primers were custom-designed and
703 ordered from Integrated DNA Technologies or Sigma-Aldrich (listed in Table S16). The thermal cycling
704 conditions were as follows: 10 minutes at 95 °C, followed by 40 cycles of 15 seconds at 95 °C and 60
705 seconds at 60 °C. Relative RNA expression levels were calculated using the comparative Ct (ΔΔCt)
706 method, normalized to the geometric mean of housekeeping genes. Fold changes were computed
707 using the 2^-ΔΔCt formula as described by Pfaffl[96], with control samples serving as the calibrator.

708

709 **Western blot analysis**

710 Synaptosomal fractions were obtained from cortical extracts from PND 60 micethe using the Syn-Per
711 reagent following manufacturer instructions as described above. Protein concentration was quantified
712 using a BCA protein assay kit (Pierce, 23225) and samples were stored at -80℃ until use. For the SDS
713 gel electrophoresis, samples were diluted in 6X Laemmli SDS buffer (375mm Tris-HCl, 9% SDS, 50%
714 glycerol, 0.03% Bromophenol blue) and 5% β-mercaptoethanol, boiled at 70℃ for 10 min, and
715 separated on a 4-20% polyacrylamide tris-glycine protein gel (BioRad). Prior loading into the gel,
716 samples were incubated at 70℃ for 10 min. After SDS-PAGE, proteins were wet transferred onto a

717 PVDF membrane (Millipore Sigma) overnight at 4℃ (13mA, constant current). Membranes were
718 blocked with Intercept PBS blocking buffer (Li-Cor) at room temperature for one hour. Primary antibody
719 PSD93 (1:50, DSHB, Clone N18/28, supernatant fraction) was diluted in 7.5 ml Intercept PBS blocking
720 buffer with 0.1% Tween. Membranes were incubated with the primary antibody solution overnight at
721 4℃, then washed four times for 10min with PBS with 0.1% Tween (PBST). Fluorescently tagged
722 secondary antibody (Li-Cor) were diluted in 10ml Intercept PBS blocking buffer with 0.1% Tween. After
723 the initial washes, blots were incubated with the secondary antibody solution for one hour at room
724 temperature. Blots were washed an additional four times for 10min with PBST and two times with PBS.
725 Bands were visualized using the Odyssey DLx imaging system (Li-Cor).
726

727 **Single Nucleus RNA-seq**

728 **Nuclei isolation for snRNA-seq and pooling strategy**

729 Frozen issue from the first 6 samples was processed into nuclei using 2mL glass dounce homogenizers
730 containing 2mL of EZ Prep lysis buffer each. Tissue for 3 samples was dounced over ice, 25 times with
731 pestle A and 35 times with pestle B. Each solution was transferred to a 15 mL conical tube, then the
732 same douncing process was repeated for the second set of 3 samples. Solutions from the latter 3
733 samples were pooled with those of the first 3 such that each pool contained one male and one female
734 of opposite genotype. An additional 6 mL of EZ Prep lysis buffer was added to each conical tube and
735 the tubes were incubated on ice for 5 minutes. Homogenates were centrifuged at 500xg for 5 minutes
736 at 4°C, the supernatant was discarded, and the pellet was washed twice in NSB (1X PBS with 0.01%
737 BSA and 0.1% RNAse inhibitor). The final pellet was resuspended in 1mL NSB then passed through a
738 20uM cell strainer. Nuclei were counted using a LUNA-FL cell counter and Acridine Orange/ Propidium
739 Iodide stain. The 10X Genomics nuclei isolation kit, with protocol as described, was used to isolate
740 nuclei for the final 4 samples. These samples were combined into 2 pools, each containing one male
741 and one female of opposite genotype, then nuclei were counted as described previously. Nuclei
742 suspensions had concentrations adjusted to target 10,000 nuclei for sequencing per pool, then used as
743 input for the 10X Genomics 3' Gene Expression Assay. Libraries were generated according to the v3

744 protocol by the UC Davis DNA Technologies Core. For the first 3 pools, libraries were sequenced with
745 the Illumina NovaSeq 6000 at 80,000 reads per nucleus. The remaining two pools were sequenced with
746 the Element Biosciences AVITI at 80,000 reads per nucleus. Raw fastq files and integrated Seurat
747 object available on GEO (GSE301511).
748

749 **RNA-seq relevant bioinformatics**

750 **Pre-processing of snRNA-seq data and initial QC**

751 De-multiplexed sequencing data were obtained from the UC Davis DNA Technologies Core as FASTQ
752 files. FASTQ files were passed through the Cell Ranger *count* pipeline for alignment to the mouse
753 mm10 genome, filtering, and creation of feature-barcode matrices. Ambient RNA removal was
754 performed using SoupX (version 1.6.1), and Seurat objects were generated using Seurat (version
755 4.3.0). These Seurat objects were subjected to initial clustering, and each resulting cluster was filtered
756 based on cluster-specific thresholds for UMI count, feature count, and percentage of mitochondrial
757 reads, which were determined using standard deviation criteria. Mitochondrial genes were then
758 removed from all objects.

759 **Doublet removal**

760 The DoubletFinder package (version 2.0.4) was used to assign nuclei as ‘Singlet’ or ‘Doublet’.
761 Predicted doublets were removed before proceeding with downstream analyses.

762 **Assigning sex and genotype**

763 Nuclei were assigned as ‘male’ or ‘female’ using a custom-built classification tool
764 (https://github.com/nickolas-chu/sxreveal) based on the expression of sex-linked marker genes located
765 on the X and Y chromosomes. *Chd8* genotype was assigned based on the predicted sex and pool-
766 specific metadata. Because each pool consisted of only one male and one female of opposite
767 genotype, all female nuclei in a pool were assumed to be one genotype and all males were assumed to
768 be the other.

769 **Clustering analysis**

770 Seurat objects for each of the 5 samples were individually passed through *SCTransform* to normalize
771 counts, then all 5 were integrated using *IntegrateData*. The 'RNA' assay of the integrated object was
772 normalized and scaled using *NormalizeData* and *ScaleData*. Principal Components Analysis was
773 performed on the 'Integrated' assay of the integrated data to identify top variable genes, and
774 *FindNeighbors* was used to construct a KNN graph based on their euclidean distance in PCA space.
775 The data were then passed through *FindClusters* to group cells into clusters using the Louvain
776 algorithm. Clusters were visualized with uniform manifold approximation and projection (UMAP).

777 **Cell type annotation**

778 *FindAllMarkers* was used to identify cluster marker genes. Modules of cell type marker genes described
779 in published scRNA-seq datasets from adult mouse cortex were constructed. Canonical marker genes
780 were added to these modules, then *AddModuleScore* was used to calculate relative expression of each
781 module in each cluster. The cell type associated with the marker gene module that had the highest
782 expression in each cluster was assigned as that cluster's identity. All nuclei were assigned identities at
783 3 levels of classification, with 'Cell_Type_1' being the most specific and 'Cell_Type_3' the broadest.

784 **Cell type re-clustering**

785 Clusters that were poorly clustered, had a high percentage of mitochondrial reads relative to other
786 clusters, or had ambiguous marker genes (i.e. markers for multiple distinct cell types) were removed
787 before subsequent analysis. The filtered Seurat object was then re-normalized, re-scaled, and re-
788 clustered as described previously.

789 **Differential expression (DE) analysis**

790 A pseudo-bulk approach was used to identify differentially-expressed genes in each cortical cell
791 population. Each cluster was extracted as a subset of the main Seurat object, then raw counts for
792 protein-coding genes were passed through the *DESeq2* pipeline to compare *Chd8* mutant and wild-type
793 nuclei within that subset. Batch was included as a covariate in the *DESeq2* statistical model. DEGs
794 with an adjusted p-value < 0.05 were deemed significant. This analysis was performed at each of the 3
795 levels of cell type assignment.

796 **Burden analysis**

797 A minimum expression threshold was determined based on the minimum expression level (‘baseMean’)
798 of DEGs with p-value < 0.05. For each cell type, DE burden was calculated as the percentage of DEGs
799 relative to the total expressed genes that passed the minimum expression threshold. A permutation test
800 with 1,000 iterations was performed to assess the statistical significance of the observed DE burden.
801 This analysis was performed at each of the three levels of cell type classification.

802 **Cell type proportion analysis**

803 For each cell population, nuclei of each genotype were counted, then counts were converted to a
804 proportion of the total cells in each sample. Linear models adjusted for genotype, sex, and batch were
805 used to assess whether or not the proportions of mutant and wild-type nuclei for each cell type were
806 statistically different.

807 **hdWGCNA**

808 High-dimensional weighted gene co-expression network analysis (hdWGCNA) was applied to construct
809 gene co-expression networks for each cell population using the hdWGCNA package (version 0.2.16).
810 Nuclei of specific cell types were grouped by sample and passed through the *MetacellsByGroups*
811 function to create metacells. Custom parameters for 'k', 'max_shared', and 'min_cells' were chosen for
812 each cell type. We determined the optimal soft power using *TestSoftPowers*, built the co-expression
813 network with *ConstructNetwork*, and detected modules via hierarchical clustering. Harmonized module
814 eigengenes (hMEs) were calculated for each module using *ModuleEigengenes* and *GetMEs*.

815 **Differential module expression analysis**

816 To test for differences in module gene expression by genotype, we analyzed each module identified in
817 glutamatergic neurons by plotting the log fold change (logFC) of its member genes based on pseudo-
818 bulk differential expression analysis. We then compared the median logFC of each module to that of
819 the corresponding 'grey' module using a t-test, applying Bonferroni correction for multiple comparisons.
820 Modules with a Bonferroni-adjusted p-value < 0.05 in at least one glutamatergic subtype were
821 considered significantly differentially expressed.

822 **GO enrichment analysis**

823 GO analysis was performed on significant DEGs and DEMs using the *enrichGO* function from the
824 clusterProfiler R package[60] (version 4.10.0), with the gene universe being set to all genes expressed in
825 the cell type the DEGs or DEMs were identified in. Genes and modules were annotated with biological
826 process and molecular function terms. Terms were deemed significant if they had a corrected p-value <
827 0.05.

828 **Gene set enrichment analysis (GSEA)**

829 Gene set enrichment analysis was performed on DEGs from bulk and pseudobulk DE analysis using
830 clusterProfiler with the org.Mm.eg.db database (version 3.18.0, Carlson M (2022). _org.Mm.eg.db:
831 Genome wide annotation for Mouse_. R package version 3.15.0.). For pseudobulk DEGs, gene hits
832 from each cell type were filtered to include only genes with adjusted p-value < 0.05 and absolute
833 LogFC > 0.25. Enrichment testing was conducted separately for upregulated and downregulated gene
834 sets using the *enrichGO* function, with background genes defined as all genes tested for differential
835 expression in the corresponding analysis. Multiple testing correction was applied using the Benjamini-
836 Hochberg method, and GO terms with adjusted p-values < 0.05 were considered significant.

837 **NeuronChat**

838 Inferred interactions were identified via the mouse database of receptor-ligand pairs and the SCT data
839 layer of the snRNAseq data. Cord diagrams show both directionality of interaction as indicated by arrow
840 direction, and the relative strength of that interaction to the others in the network via arrow line weight.
841 Aggregation across pairs was performed using the “weight” parameter. Cell-cell communication
842 strength is calculated as the product of the ligand abundance of a “sender” cell group and the target
843 abundance of a “receiver” cell group. Significance is determined by permutation test where group labels
844 of cells are randomly permuted and the communications strength is recalculated. Connection counts
845 refer to the number of non-zero sender-receiver interactions amongst cell groups. For sample level
846 differential analysis, NeuronChat[97] was run individually on each sample and the resulting metrics were
847 aggregate using mean where applicable or the replicate level data is shown. Differential strength was
848 calculated via subtractive analysis of group means, with positive values indicating increased strength in
849 the *Chd8*$^{+/-}$ group. Signaling supertypes (e.g. Glut) represent the mean aggregation of individual

interaction pairs using that ligand. Information flow refers to a weighted product incorporating number of interactions and their strengths. Output figures generated summarizing cell-cell communication were generated using NeuronChat and R.

Calcium Imaging - Stereotactic injections

We utilized adult mice of either sex housed and bred in the UCSF animal facility. To image prefrontal activity in acute slices from wildtype or mutant animals, mice were injected with AAV5.hSyn.GCaMP6f.WPRE.SV40 (Penn Viral Core). Mice were anesthetized with 2% isoflurane and mounted in a stereotactic frame. Craniotomies were made according to stereotaxic coordinates relative to Bregma. Coordinates for injection into mPFC were (in mm relative to Bregma): +1.7 anterior–posterior (AP), –0.3 mediolateral (ML) and –2.75 dorsoventral (DV). Imaging was performed 4-6 weeks later.

Slice preparation and imaging

300 µm coronal slices were prepared as previously described[98]. Immediately after preparation slices were transferred to an N-Methyl-D-Glucamine (NMDG)-based recovery solution for 10 minutes before being transferred to ACSF for the remainder of their recovery. The NMDG-based solution was maintained at 32° C, and consisted of the following (in mM): 93 N-Methyl-D-Glucamine (NMDG), 93 HCl, 2.5 KCl, 1.2 NaH2PO4, 30 NaHCO3, 25 glucose, 20 HEPES, 5 Na-ascorbate, 5 Na-pyruvate, 2 thiourea, 10 magnesium sulfate, 0.5 calcium chloride. ACSF contained the following (in mM): 126 NaCl, 26 NaHCO3, 2.5 KCl, 1.25 NaH2PO4, 1 MgCl2, 2 CaCl, and 10 glucose. For imaging slices were perfused with ‘Active’ ACSF which was identical to normal ACSF except containing elevated KCl (3.5 mM vs 2 mM) and reduced CaCl (1.2 mM vs 2 mM). Slice data was acquired at 10 Hz on an Olympus BX51 upright microscope with a 20× 1.0NA water immersion lens, 0.5× reducer (Olympus), and ORCA-ER CCD Camera (Hamamatsu Photonics). Illumination was delivered using a Lambda DG4 arc lamp (Sutter Instruments). Light was delivered through a 472/30 excitation filter, 495nm single band dichroic, and 496nm long pass emission filter (Semrock). All movies consisted of 36000 frames acquired at 10Hz

877 (1 hr) with 4×4 sensor binning yielding a final resolution of 256 × 312 pixels. Light power during imaging
878 was 100 – 500 μW/mm2. The Micro Manager software suite (v1.4, NIH) was used to control all camera
879 parameters and acquire movies. When necessary, drift correction was conducted in MATLAB using
880 custom written code[99] modified to utilize individual neurons as fiducials, whose positions were averaged
881 and aligned every 5 seconds. We segmented neuronal signals using a modified PCA/ICA approach[100]
882 modified as previously described[101] so that each segment was expressed as a binary ROI consisting of
883 pixels representing a single neuron. To deconvolve neuronal signals from background neuropil signals,
884 we subtracted the mean signal from each identified segment from the mean value in pixels surrounding
885 the edge of the segment (we excluded pixels that belonged to another ROI). Signals were subsequently
886 lowpass filtered to remove high frequency noise using the Matlab command: designfilt('lowpassfir',
887 'PassbandFrequency', 0.5, 'StopbandFrequency', .65, 'PassbandRipple', 1, 'StopbandAttenuation', 25).
888 We then detected events corresponding to epochs in which each neuron was active using threshold-
889 based event detection as previously described4. We detected increases in (F-F0)/F0 exceeding 2.5σ
890 over one frame, and then further thresholded these events by keeping only those events which
891 exceeded a 8σ increase over baseline and had an integrated area of 200 σ. σ is the standard deviation
892 of (F-F0)/F0. All further analysis was performed on binary rasters of detected events for each slice.
893

894 **Cranial Window Implantation Surgery**

895 Cranial window implantation in adult mice (6–8 weeks old) was performed as previously described[102].
896 Briefly, the mouse was anaesthetized by gaseous isoflurane (4% for induction, 1.5-2% for
897 maintenance) delivered through a vaporizer system and mounted on a stereotaxic frame. Throughout
898 the surgery the mouse was kept warm with a heating pad. Ophthalmic ointment was applied to prevent
899 eye desiccation and irritation. Carprofen (5 mg/kg, i.p.), buprenorphine (0.1 mg/kg, s.c.), enrofloxacin (5
900 mg/kg, s.c.), and dexamethasone (2 mg/kg, intramuscular) were administered. The fur over the surgical
901 site was shaved, and the scalp was cleaned with 3 rounds of alternating 70% ethanol and iodine
902 solution (Betadine®). A midline scalp incision was made, and the periosteum was gently scraped off
903 from the skull using a scalpel. A circular piece of the skull (centered at AP = –1 mm, ML = 1.5 mm) was

904 removed with a trephine (diameter = 2.3 mm, Fine Science Tools, Foster City, CA, USA) driven by a
905 high-speed micro-drill (Foredom K1070, Blackstone Industries, LLC, Bethal, CT, USA). The imaging
906 port was made by gluing a circular cover glass (#2, diameter = 2.2 mm) underneath a donut-shaped
907 glass (#1, inner diameter = 2 mm, outer diameter = 3 mm; Potomac Photonics, Inc., Baltimore, MD,
908 USA). The imaging port was mounted so that the bottom cover glass fit snugly into the cranial window
909 and the top glass donut rested above the skull. The imaging port was secured with a UV-cured
910 adhesive (Fusion Flo, Prevest DenPro, Jammu, India) onto the skull. After the solidification of the
911 adhesive, the scalp flaps were closed with suture. After 2 weeks of recovery, the central piece of the
912 scalp was excised, the edge of the scalp flap was secured to the tissue underneath with cyanoacrylate
913 (Vetbond), and a custom-made stainless-steel head-bar was secured over the skull with dental cement
914 (Jet Denture Repair, Lang Dental, Wheeling, IL, USA). The mouse received enrofloxacin,
915 buprenorphine, and carprofen once per day for two extra days post-surgery and was allowed to recover
916 for an additional week prior to imaging.
917

918 **Thin skull preparation**

919 The thin skull procedure was performed on adolescent (1 month old) mice as previously described[103].
920 Briefly, the mouse was anesthetized with a mixture of ketamine (20 mg/ml) and xylazine (2.0 mg/ml) in
921 0.9% sterile saline administered intraperitoneally (5 ml/kg body weight). Ophthalmic ointment was
922 applied to the eyes to prevent desiccation and irritation, and the fur over the scalp was removed with a
923 blade. A midline incision was made through the scalp and the periosteum was gently scraped off from
924 the skull. A high-speed micro-drill (Foredom K1070, Blackstone Industries, LLC, Bethal, CT, USA) and
925 a microblade were used to thin a small region of the skull to ~20 μm thickness. A custom-made head-
926 plate with a central opening was attached to the skull by cyanoacrylate glue (Krazy Glue, Elmer's
927 Products, Westerville, OH, USA), centered over the thinned region. The head-plate was secured onto a
928 custom-made metal baseplate to stabilize the mouse's head during imaging. Two-photon imaging was
929 performed as described above. After imaging, the head-plate was detached from the skull, the skull

930 was cleaned with sterile saline, and the scalp was sutured. The same region was imaged again 7 days
931 later.
932
933 **In vivo two-photon (2P) imaging and analysis**
934 2P imaging of dendritic spines was performed on a 2P microscope (Ultima IV, Bruker Co., Middleton,
935 WI) equipped with a 40× NA = 0.8 water immersion objective (LUMPlanFl/IR, Olympus, Japan) and an
936 ultrafast 2P laser (Mai Tai, Spectra-Physics, Santa Clara, CA) operating at 940 nm. The mouse was
937 anaesthetized with an intraperitoneal injection of a mixture of 85 mg/kg ketamine and 8.5 mg/kg
938 xylazine in 0.9% saline and mounted on a custom-made stage for imaging. Stacks of images were
939 acquired with a Z-step size of 1 μm at 4X zoom. Relocation of the same dendrites in subsequent
940 imaging sessions was achieved by reference to blood vessels and the dendritic branching pattern. The
941 same dendrites were imaged again 1 week after the first imaging session.
942 Data analysis was performed in ImageJ as previously described[103]. Typically, 150–200 spines were
943 analyzed per animal per session. The percentage of spines formed/eliminated was calculated as the
944 number of spines formed/eliminated divided by the total number of spines counted from the previous
945 imaging session. Dendritic spine density was calculated as the number of dendritic spines per 10 μm of
946 dendritic segment length on the first imaging day.
947
948 **EEG/EMG recording and analysis**
949 The EEG/EMG implant consists of a mini connector (Samtec Inc., SFMC-102-01-S-D) soldered to 2
950 EEG and 2 EMG electrodes made from Teflon-coated, multi-filament stainless steel wires (0.002” in
951 diameter, Medwire 316 SS7/44T, Sigmund Cohn Corp.). The mouse was anaesthetized by gaseous
952 isoflurane (4% for induction, 1.5-2% for maintenance) delivered through a vaporizer system and
953 mounted on a stereotaxic frame. Throughout the surgery the mouse was kept warm with a heating pad.
954 Ophthalmic ointment was applied to prevent eye desiccation and irritation. Buprenorphine (0.1 mg/kg,
955 s.c.), carprofen (5 mg/kg, i.p.), and enrofloxacin (5 mg/kg, s.c.) were injected. The fur over the surgical
956 site was shaved, and the scalp was cleaned with 3 rounds of alternating 70% ethanol and iodine

957 solution (Betadine®). A piece of the scalp was excised with scissors to expose the skull. The edge of
958 the scalp flap was secured to the tissue underneath with cyanoacrylate (Vetbond). The exposed skull
959 surface was gently scraped with a scalpel to remove the periosteum. Small holes (one at AP = + 2 mm,
960 ML = 2 mm; the other at AP = -3 mm, ML = 2 mm) were drilled through the skull using a high speed
961 microdrill (Foredom K.1070) with fine drill bits. The EEG electrodes were inserted into the holes,
962 positioned between the skull and the brain surface, and secured with a UV-curable adhesive (Fusion
963 Flo, Prevest DenPro). The EMG electrodes were positioned under the nuchal trapezoid muscles and
964 secured with Vetbond. The exposed skull surface was covered with a thin layer of Vetbond. The
965 EEG/EMG implant connector was then further secured onto the skull by dental cement (Jet Denture
966 Repair, Lang Dental). Enrofloxacin (5 mg/kg, s.c.) and carprofen (5 mg/kg, i.p.) were given at 24 h after
967 surgery. The mouse was allowed to recover for 7 days before EEG/EMG recording starts. A BL-420N
968 biological signal acquisition and processing system (Chengdu Techman, China) was used for
969 EEG/EMG recording. EEG was sampled at 200 Hz and band-pass filtered between 1-100 Hz; EMG
970 was sampled at 200 Hz and band-pass filtered between 1-2K Hz. Recorded data was annotated
971 manually and subsequently processed using custom-written Matlab programs (R2022, MathWorks
972 Inc.).

973

974 **REFERENCES**

975

976 1. Fu, J. M. *et al.* Rare coding variation provides insight into the genetic architecture and
977 phenotypic context of autism. *Nat. Genet.* **54**, 1320–1331 (2022).
978 2. Satterstrom, F. K. *et al.* Large-Scale Exome Sequencing Study Implicates Both Developmental
979 and Functional Changes in the Neurobiology of Autism. *Cell* **180**, 568-584.e23 (2020).
980 3. Alotaibi, M. & Ramzan, K. A de novo variant of CHD8 in a patient with autism spectrum
981 disorder. *Discov. Craiova Rom.* **8**, e107 (2020).
982 4. An, Y. *et al.* De novo variants in the Helicase-C domain of CHD8 are associated with severe
983 phenotypes including autism, language disability and overgrowth. *Hum. Genet.* **139**, 499–512
984 (2020).
985 5. Beighley, J. S. *et al.* Clinical Phenotypes of Carriers of Mutations in CHD8 or Its Conserved
986 Target Genes. *Biol. Psychiatry* **87**, 123–131 (2020).
987 6. Bernier, R. *et al.* Disruptive CHD8 Mutations Define a Subtype of Autism Early in Development.
988 *Cell* **158**, 263–276 (2014).
989 7. Doummar, D. *et al.* Childhood-onset progressive dystonia associated with pathogenic
990 truncating variants in CHD8. *Ann. Clin. Transl. Neurol.* **8**, 1986–1990 (2021).
991 8. Douzgou, S. *et al.* The clinical presentation caused by truncating CHD8 variants. *Clin. Genet.*
992 **96**, 72–84 (2019).
993 9. Ostrowski, P. J. *et al.* The CHD8 overgrowth syndrome: A detailed evaluation of an emerging
994 overgrowth phenotype in 27 patients. *Am. J. Med. Genet. C Semin. Med. Genet.* **181**, 557–564
995 (2019).
996 10. Amaral, D. G. *et al.* In pursuit of neurophenotypes: The consequences of having autism and a
997 big brain. *Autism Res. Off. J. Int. Soc. Autism Res.* **10**, 711–722 (2017).

998 11. Barnard, R. A., Pomaville, M. B. & O'Roak, B. J. Mutations and Modeling of the Chromatin
999 Remodeler CHD8 Define an Emerging Autism Etiology. *Front. Neurosci.* **9**, (2015).
1000 12. Cotney, J. *et al.* The autism-associated chromatin modifier CHD8 regulates other autism risk
1001 genes during human neurodevelopment. *Nat. Commun.* **6**, 6404 (2015).
1002 13. Willsey, H. R., Willsey, A. J., Wang, B. & State, M. W. Genomics, convergent neuroscience and
1003 progress in understanding autism spectrum disorder. *Nat. Rev. Neurosci.* **23**, 323–341 (2022).
1004 14. Levy, D. *et al.* Rare De Novo and Transmitted Copy-Number Variation in Autistic Spectrum
1005 Disorders. *Neuron* **70**, 886–897 (2011).
1006 15. O'Roak, B. J. *et al.* Sporadic autism exomes reveal a highly interconnected protein network of
1007 de novo mutations. *Nature* **485**, 246–250 (2012).
1008 16. O'Roak, B. J. *et al.* Exome sequencing in sporadic autism spectrum disorders identifies severe
1009 de novo mutations. *Nat. Genet.* **43**, 585–589 (2011).
1010 17. Ronemus, M., Iossifov, I., Levy, D. & Wigler, M. The role of de novo mutations in the genetics of
1011 autism spectrum disorders. *Nat. Rev. Genet.* **15**, 133–141 (2014).
1012 18. Yuen, R. K. *et al.* Genome-wide characteristics of de novo mutations in autism. *Npj Genomic*
1013 *Med.* **1**, 1–10 (2016).
1014 19. Nishiyama, M. *et al.* Early Embryonic Death in Mice Lacking the β-Catenin-Binding Protein
1015 Duplin. *Mol. Cell. Biol.* **24**, 8386–8394 (2004).
1016 20. Gompers, A. L. *et al.* Germline Chd8 haploinsufficiency alters brain development in mouse.
1017 *Nat. Neurosci.* **20**, 1062–1073 (2017).
1018 21. Jung, H. *et al.* Sexually dimorphic behavior, neuronal activity, and gene expression in Chd8-
1019 mutant mice. *Nat. Neurosci.* **21**, 1218–1228 (2018).

1020 22. Katayama, Y. *et al.* CHD8 haploinsufficiency results in autistic-like phenotypes in mice.
1021 *Nature* **537**, 675–679 (2016).
1022 23. Niu, X. *et al.* The Deficiency of the ASD-Related Gene CHD8 Disrupts Behavioral Patterns and
1023 Inhibits Hippocampal Neurogenesis in Mice. *J. Mol. Neurosci. MN* **74**, 103 (2024).
1024 24. Platt, R. J. *et al.* Chd8 Mutation Leads to Autistic-like Behaviors and Impaired Striatal Circuits.
1025 *Cell Rep.* **19**, 335–350 (2017).
1026 25. Suetterlin, P. *et al.* Altered Neocortical Gene Expression, Brain Overgrowth and Functional
1027 Over-Connectivity in Chd8 Haploinsufficient Mice. *Cereb. Cortex N. Y. N 1991* **28**, 2192–2206
1028 (2018).
1029 26. Jiménez, J. A. *et al.* Chd8 haploinsufficiency impairs early brain development and protein
1030 homeostasis later in life. *Mol. Autism* **11**, 74 (2020).
1031 27. Jiménez, J. A. *et al.* Chd8 haploinsufficiency impairs early brain development and protein
1032 homeostasis later in life. *Mol. Autism* **11**, 74 (2020).
1033 28. Durak, O. *et al.* Chd8 mediates cortical neurogenesis via transcriptional regulation of cell
1034 cycle and Wnt signaling. *Nat. Neurosci.* **19**, 1477–1488 (2016).
1035 29. Yim, K. M. *et al.* Cell type-specific dysregulation of gene expression due to Chd8
1036 haploinsufficiency during mouse cortical development. *bioRxiv* 2024.08.14.608000 (2024)
1037 doi:10.1101/2024.08.14.608000.
1038 30. Hurley, S. *et al.* Distinct, dosage-sensitive requirements for the autism-associated factor
1039 CHD8 during cortical development. *Mol. Autism* **12**, 16 (2021).
1040 31. Astorkia, M., Liu, Y., Pedrosa, E. M., Lachman, H. M. & Zheng, D. Molecular and network
1041 disruptions in neurodevelopment uncovered by single cell transcriptomics analysis of CHD8

1042 heterozygous cerebral organoids. Preprint at https://doi.org/10.1101/2023.09.27.559752
1043 (2023).
1044 32. Paulsen, B. *et al.* Autism genes converge on asynchronous development of shared neuron
1045 classes. *Nature* **602**, 268–273 (2022).
1046 33. Hoffmann, A. & Spengler, D. Single-Cell Transcriptomics Supports a Role of CHD8 in Autism.
1047 *Int. J. Mol. Sci.* **22**, 3261 (2021).
1048 34. Tabbaa, M., Knoll, A. & Levitt, P. Mouse population genetics phenocopies heterogeneity of
1049 human Chd8 haploinsufficiency. *Neuron* **111**, 539-556.e5 (2023).
1050 35. Tabbaa, M. & Levitt, P. Chd8 haploinsufficiency impacts rearing experience in C57BL/6 mice.
1051 *Genes Brain Behav.* **23**, e12892 (2024).
1052 36. Ellingford, R. A. *et al.* Cell-type-specific synaptic imbalance and disrupted homeostatic
1053 plasticity in cortical circuits of ASD-associated Chd8 haploinsufficient mice. *Mol. Psychiatry*
1054 **26**, 3614–3624 (2021).
1055 37. Ellingford, R. A., Tojo, M., Basson, M. A. & Andreae, L. C. Male-Dominant Effects of Chd8
1056 Haploinsufficiency on Synaptic Phenotypes during Development in Mouse Prefrontal Cortex.
1057 *ACS Chem. Neurosci.* **15**, 1635–1642 (2024).
1058 38. Villa, C. E. *et al.* CHD8 haploinsufficiency links autism to transient alterations in excitatory
1059 and inhibitory trajectories. *Cell Rep.* **39**, 110615 (2022).
1060 39. Li, B. *et al.* CHD8 mutations increase gliogenesis to enlarge brain size in the nonhuman
1061 primate. *Cell Discov.* **9**, 27 (2023).
1062 40. Shi, X. *et al.* Heterozygous deletion of the autism-associated gene CHD8 impairs synaptic
1063 function through widespread changes in gene expression and chromatin compaction. *Am. J.*
1064 *Hum. Genet.* **110**, 1750–1768 (2023).

1065 41. Gao, Y. *et al.* Multimodal analyses reveal genes driving electrophysiological maturation of
1066 neurons in the primate prefrontal cortex. Preprint at
1067 https://doi.org/10.1101/2023.06.02.543460 (2024).
1068 42. Kweon, H. *et al.* Excitatory neuronal CHD8 in the regulation of neocortical development and
1069 sensory-motor behaviors. *Cell Rep.* **34**, 108780 (2021).
1070 43. Haddad Derafshi, B. *et al.* The autism risk factor CHD8 is a chromatin activator in human
1071 neurons and functionally dependent on the ERK-MAPK pathway effector ELK1. *Sci. Rep.* **12**,
1072 22425 (2022).
1073 44. Kawamura, A. & Nishiyama, M. Deletion of the autism-related gene Chd8 alters activity-
1074 dependent transcriptional responses in mouse postmitotic neurons. *Commun. Biol.* **6**, 593
1075 (2023).
1076 45. Dong, C. *et al.* Conserved and Distinct Functions of the Autism-Related Chromatin Remodeler
1077 CHD8 in Embryonic and Adult Forebrain Neurogenesis. *J. Neurosci. Off. J. Soc. Neurosci.* **42**,
1078 8373–8392 (2022).
1079 46. Chen, X. *et al.* Deletion of CHD8 in cerebellar granule neuron progenitors leads to severe
1080 cerebellar hypoplasia, ataxia, and psychiatric behavior in mice. *J. Genet. Genomics Yi Chuan*
1081 *Xue Bao* **49**, 859–869 (2022).
1082 47. Kawamura, A. *et al.* Oligodendrocyte dysfunction due to Chd8 mutation gives rise to
1083 behavioral deficits in mice. *Hum. Mol. Genet.* **29**, 1274–1291 (2020).
1084 48. Kawamura, A. *et al.* Chd8 mutation in oligodendrocytes alters microstructure and functional
1085 connectivity in the mouse brain. *Mol. Brain* **13**, 160 (2020).

1086 49. Zhao, C. *et al.* Dual Requirement of CHD8 for Chromatin Landscape Establishment and
1087 Histone Methyltransferase Recruitment to Promote CNS Myelination and Repair. *Dev. Cell* **45**,
1088 753-768.e8 (2018).
1089 50. Megagiannis, P. *et al.* Autism-associated CHD8 controls reactive gliosis and
1090 neuroinflammation via remodeling chromatin in astrocytes. *Cell Rep.* **43**, 114637 (2024).
1091 51. Takanezawa, Y. *et al.* Microglial ASD-related genes are involved in oligodendrocyte
1092 differentiation. *Sci. Rep.* **11**, 17825 (2021).
1093 52. Spear, L. P. The adolescent brain and age-related behavioral manifestations. *Neurosci.*
1094 *Biobehav. Rev.* **24**, 417–463 (2000).
1095 53. West, M. J. & Gundersen, H. J. Unbiased stereological estimation of the number of neurons in
1096 the human hippocampus. *J. Comp. Neurol.* **296**, 1–22 (1990).
1097 54. Lavenex, P. B. Lesions in the budgerigar vocal control nucleus NLc affect production, but not
1098 memory, of english words and natural vocalizations. *J. Comp. Neurol.* **421**, 437–460 (2000).
1099 55. West, M. J., Slomianka, L. & Gundersen, H. J. Unbiased stereological estimation of the total
1100 number of neurons in thesubdivisions of the rat hippocampus using the optical fractionator.
1101 *Anat. Rec.* **231**, 482–497 (1991).
1102 56. Young, M. D. & Behjati, S. SoupX removes ambient RNA contamination from droplet-based
1103 single-cell RNA sequencing data. *GigaScience* **9**, giaa151 (2020).
1104 57. Yao, Z. *et al.* A high-resolution transcriptomic and spatial atlas of cell types in the whole
1105 mouse brain. *BioRxiv Prepr. Serv. Biol.* 2023.03.06.531121 (2023)
1106 doi:10.1101/2023.03.06.531121.
1107 58. Murphy, A. E. & Skene, N. G. A balanced measure shows superior performance of pseudobulk
1108 methods in single-cell RNA-sequencing analysis. *Nat. Commun.* **13**, 7851 (2022).

1109 59. Love, M. I., Huber, W. & Anders, S. Moderated estimation of fold change and dispersion for
1110 RNA-seq data with DESeq2. *Genome Biol.* **15**, 1–21 (2014).
1111 60. Wu, T. *et al.* clusterProfiler 4.0: A universal enrichment tool for interpreting omics data. *Innov.*
1112 *Camb. Mass* **2**, 100141 (2021).
1113 61. Morabito, S., Reese, F., Rahimzadeh, N., Miyoshi, E. & Swarup, V. hdWGCNA identifies co-
1114 expression networks in high-dimensional transcriptomics data. *Cell Rep. Methods* **3**, 100498
1115 (2023).
1116 62. Robinson, M. D., McCarthy, D. J. & Smyth, G. K. edgeR: a Bioconductor package for differential
1117 expression analysis of digital gene expression data. *Bioinforma. Oxf. Engl.* **26**, 139–140 (2010).
1118 63. Yoo, T. *et al.* A DLG2 deficiency in mice leads to reduced sociability and increased repetitive
1119 behavior accompanied by aberrant synaptic transmission in the dorsal striatum. *Mol. Autism*
1120 **11**, 19 (2020).
1121 64. Yoo, T. *et al.* A Deficiency of the Psychiatric Risk Gene DLG2/PSD-93 Causes Excitatory
1122 Synaptic Deficits in the Dorsolateral Striatum. *Front. Mol. Neurosci.* **15**, 938590 (2022).
1123 65. Sanders, B. *et al.* Transcriptional programs regulating neuronal differentiation are disrupted in
1124 DLG2 knockout human embryonic stem cells and enriched for schizophrenia and related
1125 disorders risk variants. *Nat. Commun.* **13**, 27 (2022).
1126 66. Chang, X. *et al.* Common and Rare Genetic Risk Factors Converge in Protein Interaction
1127 Networks Underlying Schizophrenia. *Front. Genet.* **9**, 434 (2018).
1128 67. Feng, G. *et al.* Imaging neuronal subsets in transgenic mice expressing multiple spectral
1129 variants of GFP. *Neuron* **28**, 41–51 (2000).

1130 68. Wang, P. *et al.* CRISPR/Cas9-mediated heterozygous knockout of the autism gene CHD8 and
1131 characterization of its transcriptional networks in neurodevelopment. *Mol. Autism* **6**, 55
1132 (2015).
1133 69. Haddad Derafshi, B. *et al.* The autism risk factor CHD8 is a chromatin activator in human
1134 neurons and functionally dependent on the ERK-MAPK pathway effector ELK1. *Sci. Rep.* **12**,
1135 22425 (2022).
1136 70. Earl, R. K. *et al.* Sleep Problems in Children with ASD and Gene Disrupting Mutations. *J. Genet.*
1137 *Psychol.* **182**, 317–334 (2021).
1138 71. topGO. *Bioconductor* http://bioconductor.org/packages/topGO/.
1139 72. Kerschbamer, E. *et al.* CHD8 suppression impacts on histone H3 lysine 36 trimethylation and
1140 alters RNA alternative splicing. *Nucleic Acids Res.* **50**, 12809–12828 (2022).
1141 73. Wade, A. A., Lim, K., Catta-Preta, R. & Nord, A. S. Common CHD8 Genomic Targets Contrast
1142 With Model-Specific Transcriptional Impacts of CHD8 Haploinsufficiency. *Front. Mol.*
1143 *Neurosci.* **11**, 481 (2018).
1144 74. Ashley, C. T., Wilkinson, K. D., Reines, D. & Warren, S. T. FMR1 Protein: Conserved RNP Family
1145 Domains and Selective RNA Binding. *Science* **262**, 563–566 (1993).
1146 75. Ascano, M. *et al.* FMRP targets distinct mRNA sequence elements to regulate protein
1147 expression. *Nature* **492**, 382–386 (2012).
1148 76. Sun, N. *et al.* Autism genes converge on microtubule biology and RNA-binding proteins during
1149 excitatory neurogenesis. 2023.12.22.573108 Preprint at
1150 https://doi.org/10.1101/2023.12.22.573108 (2024).
1151 77. Parikshak, N. N. *et al.* Genome-wide changes in lncRNA, splicing, and regional gene
1152 expression patterns in autism. *Nature* **540**, 423–427 (2016).

1153 78. Zaghlool, A. *et al*. Characterization of the nuclear and cytosolic transcriptomes in human
1154 brain tissue reveals new insights into the subcellular distribution of RNA transcripts. *Sci. Rep*.
1155 **11**, 4076 (2021).
1156 79. Bakken, T. E. *et al*. Single-nucleus and single-cell transcriptomes compared in matched
1157 cortical cell types. *PloS One* **13**, e0209648 (2018).
1158 80. Squair, J. W. *et al*. Confronting false discoveries in single-cell differential expression. *Nat*.
1159 *Commun*. **12**, 5692 (2021).
1160 81. Chareyron, L. J., Banta Lavenex, P., Amaral, D. G. & Lavenex, P. Stereological analysis of the
1161 rat and monkey amygdala. *J. Comp. Neurol*. **519**, 3218–3239 (2011).
1162 82. Lavenex, P., Lavenex, P. B., Bennett, J. L. & Amaral, D. G. Postmortem changes in the
1163 neuroanatomical characteristics of the primate brain: hippocampal formation. *J. Comp*.
1164 *Neurol*. **512**, 27–51 (2009).
1165 83. *Paxinos and Franklin's the Mouse Brain in Stereotaxic Coordinates*. (2019).
1166 84. Gundersen, H. J. & Jensen, E. B. The efficiency of systematic sampling in stereology and its
1167 prediction. *J. Microsc*. **147**, 229–263 (1987).
1168 85. Gundersen, H. J. Stereology of arbitrary particles. A review of unbiased number and size
1169 estimators and the presentation of some new ones, in memory of William R. Thompson. *J.*
1170 *Microsc*. **143**, 3–45 (1986).
1171 86. Long, J. M. *et al*. Stereological estimation of total microglia number in mouse hippocampus. *J.*
1172 *Neurosci. Methods* **84**, 101–108 (1998).
1173 87. García-Cabezas, M. Á., John, Y. J., Barbas, H. & Zikopoulos, B. Distinction of Neurons, Glia and
1174 Endothelial Cells in the Cerebral Cortex: An Algorithm Based on Cytological Features. *Front*.
1175 *Neuroanat*. **10**, 107 (2016).

1176 88. Haida, O. *et al*. Sex-dependent behavioral deficits and neuropathology in a maternal immune
1177 activation model of autism. *Transl. Psychiatry* **9**, 124 (2019).
1178 89. Lauber, E., Filice, F. & Schwaller, B. Dysregulation of Parvalbumin Expression in the Cntnap2-
1179 /- Mouse Model of Autism Spectrum Disorder. *Front. Mol. Neurosci.* **11**, 262 (2018).
1180 90. Gundersen, H. J. The nucleator. *J. Microsc.* **151**, 3–21 (1988).
1181 91. Wickham, H. *Ggplot2: Elegant Graphics for Data Analysis*. (Springer, New York, NY, 2009).
1182 doi:10.1007/978-0-387-98141-3.
1183 92. Dobin, A. *et al*. STAR: ultrafast universal RNA-seq aligner. *Bioinforma. Oxf. Engl.* **29**, 15–21
1184 (2013).
1185 93. Liao, Y., Smyth, G. K. & Shi, W. featureCounts: an efficient general purpose program for
1186 assigning sequence reads to genomic features. *Bioinforma. Oxf. Engl.* **30**, 923–930 (2014).
1187 94. Babraham Bioinformatics - FastQC A Quality Control tool for High Throughput Sequence Data.
1188 https://www.bioinformatics.babraham.ac.uk/projects/fastqc/.
1189 95. Leek, J. T., Johnson, W. E., Parker, H. S., Jaffe, A. E. & Storey, J. D. The sva package for
1190 removing batch effects and other unwanted variation in high-throughput experiments.
1191 *Bioinforma. Oxf. Engl.* **28**, 882–883 (2012).
1192 96. Pfaffl, M. W. A new mathematical model for relative quantification in real-time RT-PCR.
1193 *Nucleic Acids Res.* **29**, e45 (2001).
1194 97. Zhao, W., Johnston, K. G., Ren, H., Xu, X. & Nie, Q. Inferring neuron-neuron communications
1195 from single-cell transcriptomics through NeuronChat. *Nat. Commun.* **14**, 1128 (2023).
1196 98. Luongo, F. J., Horn, M. E. & Sohal, V. S. Putative Microcircuit-Level Substrates for Attention Are
1197 Disrupted in Mouse Models of Autism. *Biol. Psychiatry* **79**, 667–675 (2016).

1198 99. Frost, N. A., Shroff, H., Kong, H., Betzig, E. & Blanpied, T. A. Single-molecule discrimination of
1199 discrete perisynaptic and distributed sites of actin filament assembly within dendritic spines.
1200 *Neuron* **67**, 86–99 (2010).
1201 100. Mukamel, E. A., Nimmerjahn, A. & Schnitzer, M. J. Automated analysis of cellular signals
1202 from large-scale calcium imaging data. *Neuron* **63**, 747–760 (2009).
1203 101. Frost, N. A., Haggart, A. & Sohal, V. S. Dynamic patterns of correlated activity in the
1204 prefrontal cortex encode information about social behavior. *PLoS Biol.* **19**, e3001235 (2021).
1205 102. Lu, J. *et al.* An analog of psychedelics restores functional neural circuits disrupted by
1206 unpredictable stress. *Mol. Psychiatry* **26**, 6237–6252 (2021).
1207 103. Xu, T. *et al.* Rapid formation and selective stabilization of synapses for enduring motor
1208 memories. *Nature* **462**, 915–919 (2009).
1209

A

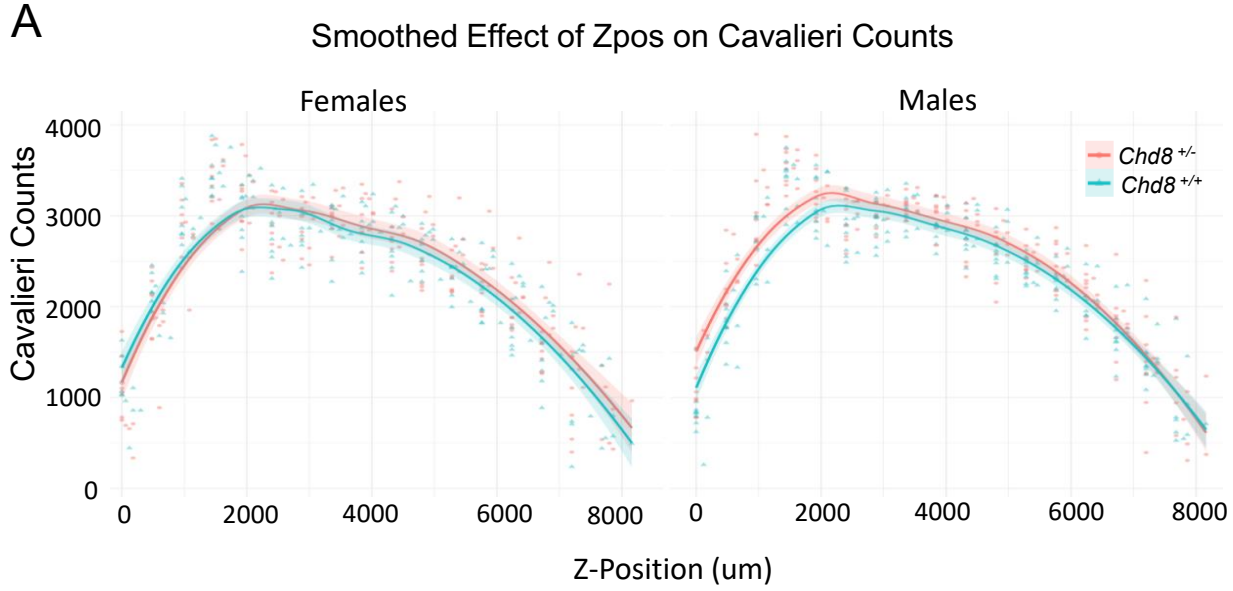
Smoothed Effect of Zpos on Cavalieri Counts
Females
Males
Cavalieri Counts
4000
3000
2000
1000
0
0
2000
4000
6000
8000
Chd8 +/-
Chd8 +/+
Z-Position (um)

B

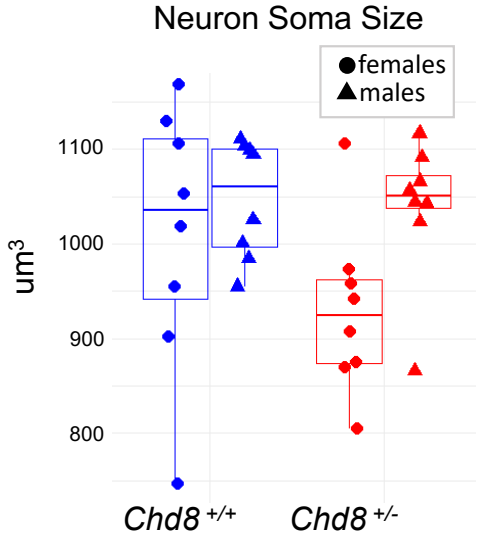
Neuron Soma Size
females
males
um3
1100
1000
900
800
Chd8 +/+
Chd8 +/-

1

Figure S1: A) Cortical volume was quantified across rostral–caudal section in *Chd8*$^{+/-}$ and *Chd8*$^{+/+}$ mice using the Cavalieri method. In male *Chd8*$^{+/-}$ mice, increased volume was observed predominantly in more rostral regions, with clearer separation of genotype averages along the anterior Z-positions. Shaded portions of the plots indicate the more caudal regions (0–3000 µm), where volume differences are most evident. B) Neuronal soma size, measured by unbiased stereology in the same rostro-caudal range, did not differ significantly between genotypes. Data are stratified by sex and genotype. Error bars represent SEM. Statistical comparisons were performed using two-way ANOVA (unstratified: P = 0.23; males: P = 0.81; females: P = 0.19).

A Representative QC plot

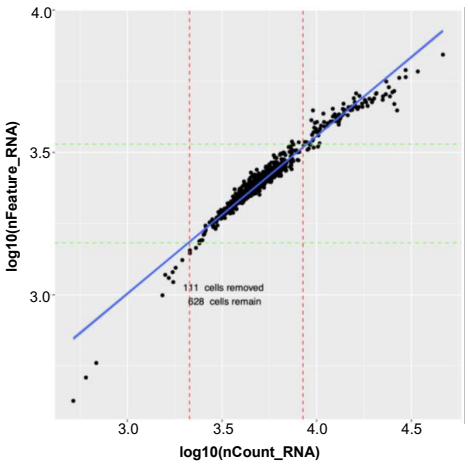

B Integration with BICCN data for cell type assignment

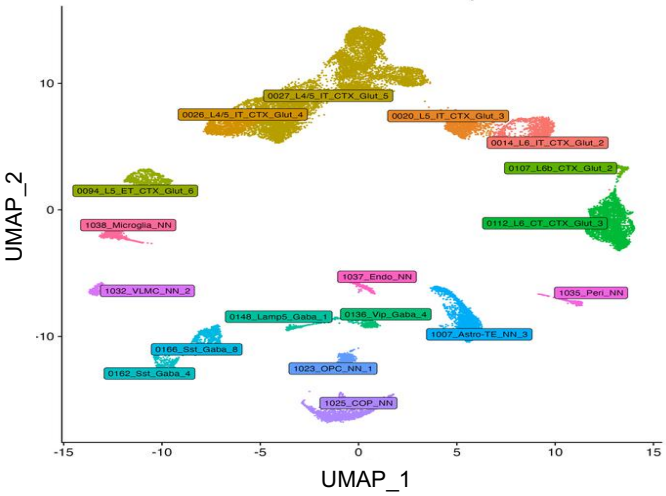

C Representative sex-stratified DE concordance

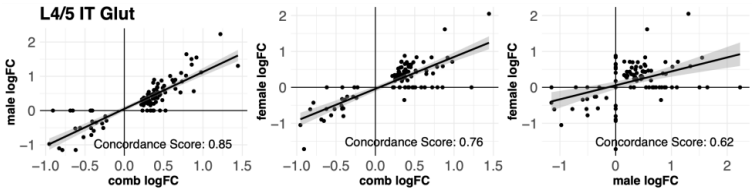

D Representative no soupx DE concordance

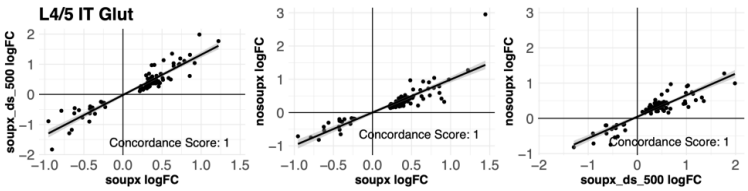

E Downsampled and nosoupx DE burden

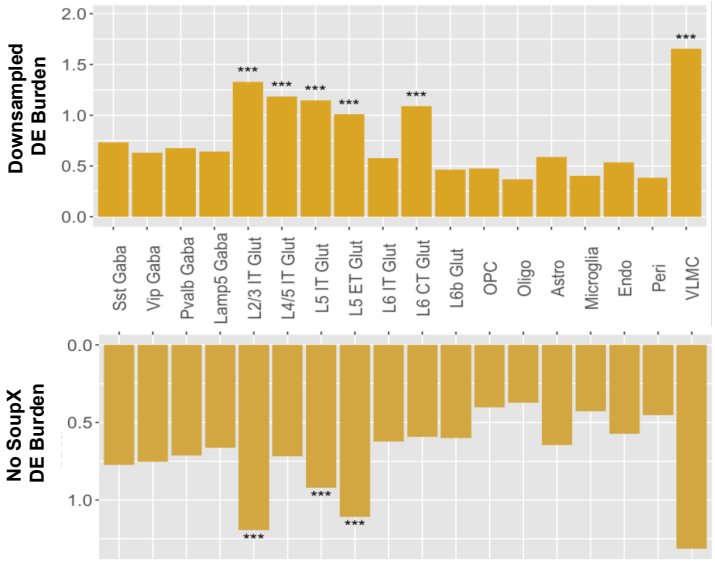

F Pseudobulk DE GSEA

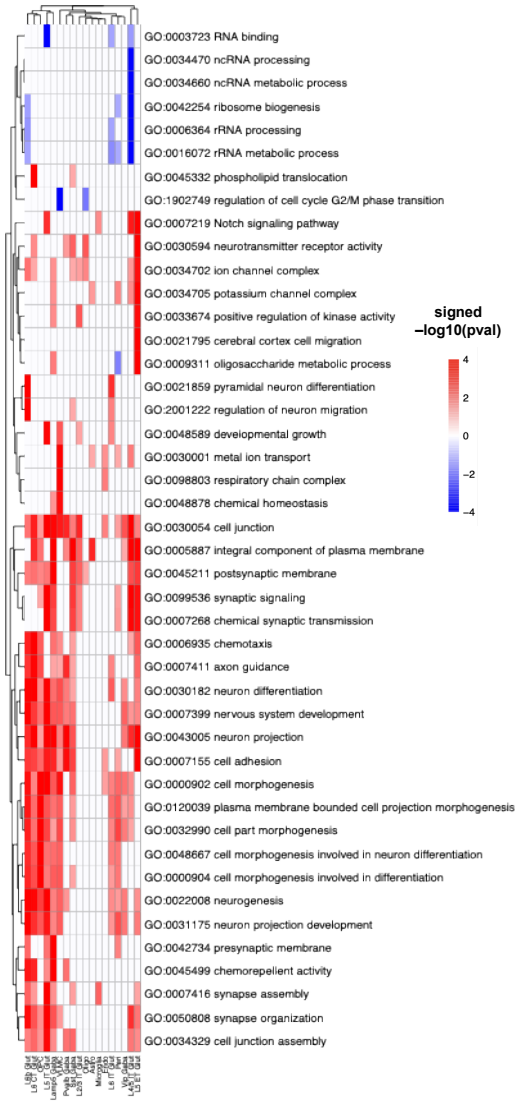

10

Figure S2: A) Scatterplot of log10-transformed total RNA counts (nCount_RNA) versus detected genes (nFeature_RNA) per cell in one batch. Custom MAD-based thresholds were chosen per batch to filter low-quality cells. Red and green dotted lines indicate nCount_RNA and nFeature_RNA cutoffs, respectively; cells outside these thresholds were excluded from downstream analysis. B) UMAP showing all *Chd8* mutant and wild-type nuclei integrated with BICCN data and annotated with predicted BICCN cell type labels, which are consistent with cell type identities derived from our independent annotation pipeline. C) Scatterplots comparing log fold changes (logFC) of the top 100 DEGs identified with full SoupX, non-downsampled DE analysis (“soupx”) to their logFCs in the no-SoupX (“nosoupx”) and downsampled to 500 nuclei + SoupX (“soupx_ds_500”) analyses for a representative cell type. Concordance scores were calculated as the proportion of genes with the same direction of change between methods. D) Scatterplots comparing logFC of the top 100 DEGs identified with male-and-female-combined (“comb”) DE analysis to their logFCs in the male and female DE analyses for a representative cell type. E) Bar plots of DEG burden across cell types (Burden = DE genes / total genes expressed * 100) for downsampled (top) and no-SoupX (bottom) DE analyses. A permutation test with 10,000 iterations was used to assess statistical significance and confirmed that the observed trends were similar to those in the full SoupX, non-downsampled analysis. F) Heatmap of normalized enrichment scores (NES) for a curated set of biologically relevant GO terms identified by GSEA performed on pseudobulk DEGs for each cell type.

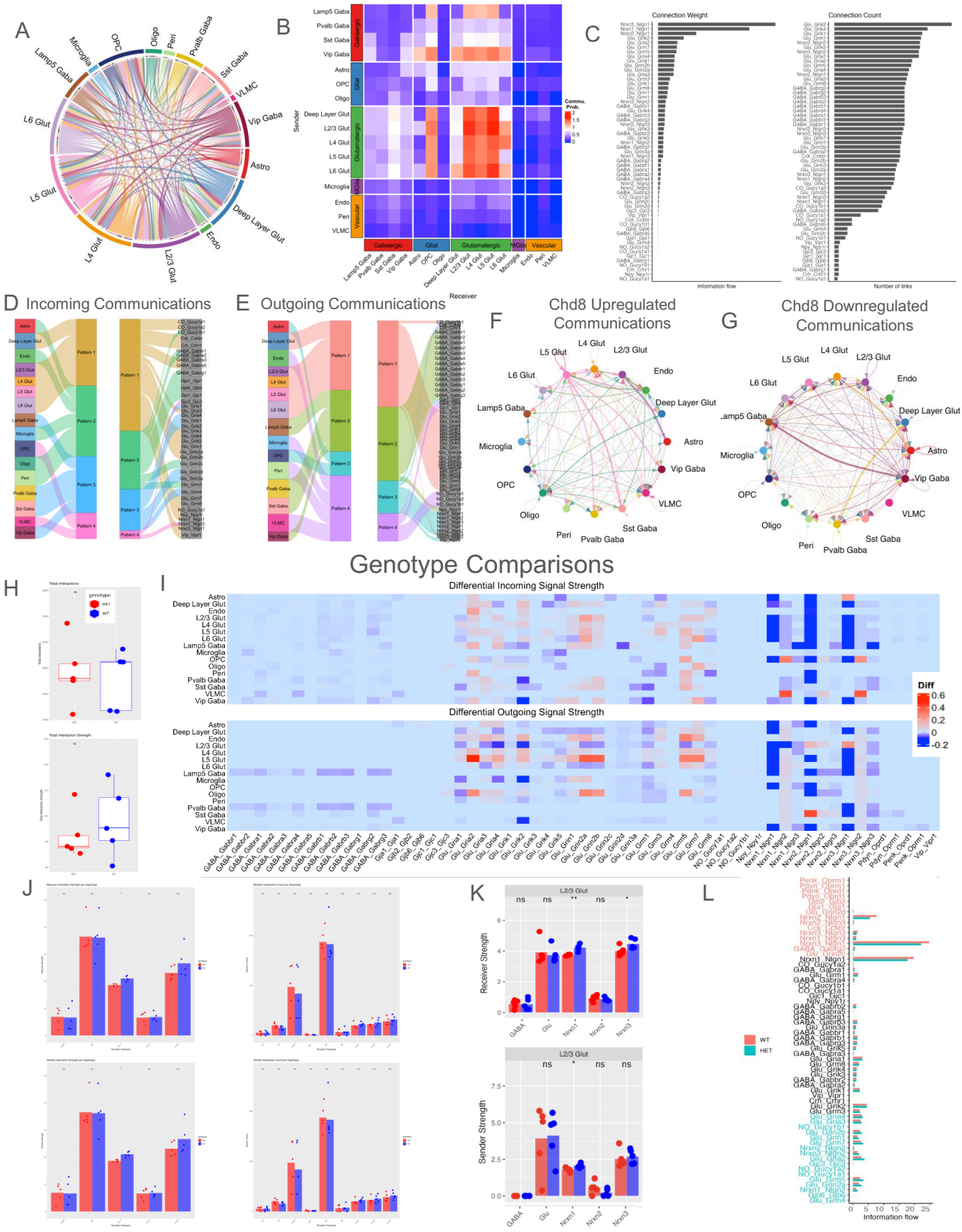
A
B
C
Connection Weight
Connection Count
Information flow
Number of links
Sender
Receiver
Commu. Prob.
D Incoming Communications
E Outgoing Communications
F Chd8 Upregulated Communications
G Chd8 Downregulated Communications
Genotype Comparisons
H
I
Differential Incoming Signal Strength
Differential Outgoing Signal Strength
Diff
J
K
L
L2/3 Glut
Receiver Strength
Sender Strength
WT
HET
Information flow

Figure S3: A) Overview of all inferred connections by cell type shows generally balanced co-directional signaling for each cell type. B) The communication probability is strongest within Glutamatergic cell types and between Glutamatergic and GABAergic populations. C) The strength and count of connections anchored by the listed receptor highlight networking drivers. D, E) Cell types are grouped based on the similarity of their incoming or outgoing connections showing similarities correlated with similar cell identities and neurotransmitter types. F, G) Circle plots showing the upregulated (F) and downregulated (G) intercellular communications in *Chd8*$^{+/-}$ compared to control. The width of each link indicates the absolute difference between Chd8 and control, in the sum of communication strength values over all interaction pairs. H) The relative strength (top) of all network connections is similar in both WT and *Chd8*$^{+/-}$ ("HET") animals but the number of connections (bottom) shows some elevation in the *Chd8*$^{+/-}$ animals. I) Heatmap showing the differential outgoing (upper panel) and incoming (lower panel) signal strength between *Chd8*$^{+/-}$ and control. Given the cell group and interaction pair, the outgoing (or incoming) signal strength is defined as the sum of communication strength over the links from (or to) the cell group. The color bar indicates the difference in the outgoing (or incoming) signal strength values between *Chd8*$^{+/-}$ and control. Interaction pairs with signal strength of 0 for all cell types were omitted from plotting. J) Replicate level quantification of receptor supertype sender (top) and receiver (bottom) differences shows dysregulation only in the Nrxn1 strength metrics on the level of the entire dataset. K) Further cell type specific inspection indicates that the L2/3 population is the only significantly affected population driving the dysregulation. L) Bar chart comparing the information flow between *Chd8*$^{+/-}$ and control for each interaction pair at the full dataset level. While the HET samples show both decreased and increased information flow in some interaction pairs, those that are increased have a vastly greater magnitude thus dominating the effects. In contrast, the increased information flow seen in the glutamate interactions is present in connections with decreased overall magnitude but is considerably consistent across each glutamate-receptor-ligand pair and reveals the glutamate network dominating the rankings of information flow increases in the HET.

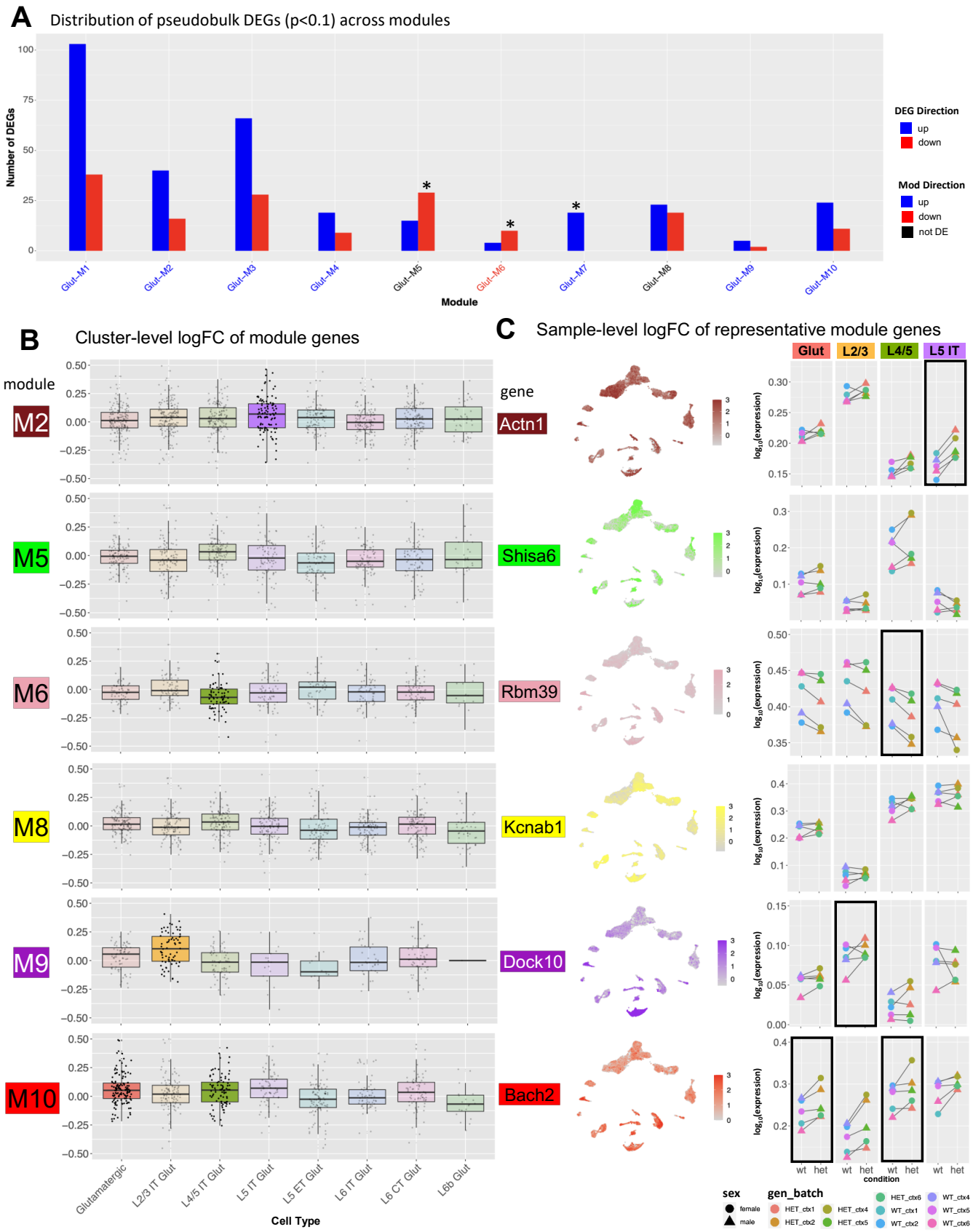
A
Distribution of pseudobulk DEGs (p<0.1) across modules
Number of DEGs
Module
Glut-M1
Glut-M2
Glut-M3
Glut-M4
Glut-M5
Glut-M6
Glut-M7
Glut-M8
Glut-M9
Glut-M10
DEG Direction
up
down
Mod Direction
up
down
not DE
B
Cluster-level logFC of module genes
module
M2
M5
M6
M8
M9
M10
Glutamatergic
L2/3 IT Glut
L4/5 IT Glut
L5 IT Glut
L5 ET Glut
L6 IT Glut
L6 CT Glut
L6b Glut
Cell Type
C
Sample-level logFC of representative module genes
gene
Actn1
Shisa6
Rbm39
Kcnab1
Dock10
Bach2
Glut
L2/3
L4/5
L5 IT
log10(expression)
wt
het
condition
sex
female
male
gen_batch
HET_ctx1
HET_ctx2
HET_ctx4
HET_ctx5
HET_ctx6
WT_ctx1
WT_ctx2
WT_ctx4
WT_ctx5
WT_ctx6

55

Figure S4: A) Bar plot showing the distribution of DEGs ($p < 0.1$) across glutamatergic modules. Bars indicate the number of genes upregulated (blue) or downregulated (red) in at least one cell type per module. Modules Glut-M5 and Glut-M6 showed significant enrichment for downregulated DEGs (Fisher's exact test, FDR-adjusted $*p < 0.05$), while Glut-M7 showed significant enrichment for upregulated DEGs. Overall, the direction of module-level change tends to agree with the predominant direction of DE for the genes within each module. B) Box plots for the remaining glutamatergic modules, showing logFCs of module genes across cell types. Opaque boxes indicate subtypes where the module is significantly differentially expressed (Student's t-test comparing mean logFC of each module to grey module, Bonferroni-adjusted $p < 0.05$). C) Feature plots (left) show relative expression of representative genes from each module in UMAP space. Dot plots (right) display median sample-level expression of the same genes. Black boxes highlight subtypes where the module is differentially expressed or where consistent directional changes are observed across batches.

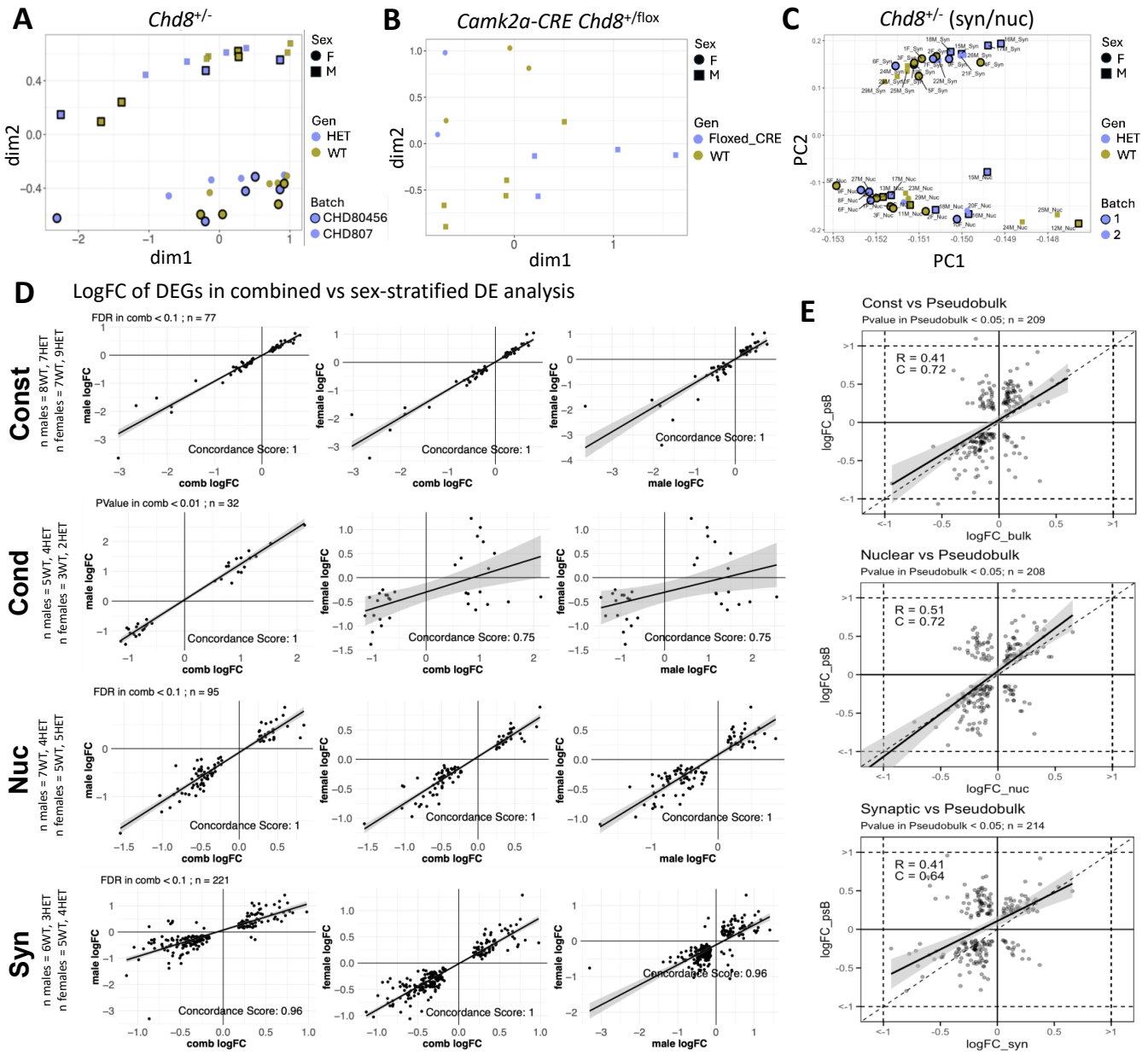
A
Chd8+/-
dim2
dim1
Sex
F
M
Gen
HET
WT
Batch
CHD80456
CHD807
B
Camk2a-CRE Chd8+/flox
dim2
dim1
Sex
F
M
Gen
Floxed_CRE
WT
C
Chd8+/- (syn/nuc)
PC2
PC1
Sex
F
M
Gen
HET
WT
Batch
1
2
D
LogFC of DEGs in combined vs sex-stratified DE analysis
Const
n males = 8WT, 7HET
n females = 7WT, 9HET
FDR in comb < 0.1 ; n = 77
Concordance Score: 1
Concordance Score: 1
Concordance Score: 1
Cond
n males = 5WT, 4HET
n females = 3WT, 2HET
PValue in comb < 0.01 ; n = 32
Concordance Score: 1
Concordance Score: 0.75
Concordance Score: 0.75
Nuc
n males = 7WT, 4HET
n females = 5WT, 5HET
FDR in comb < 0.1 ; n = 95
Concordance Score: 1
Concordance Score: 1
Concordance Score: 1
Syn
n males = 6WT, 3HET
n females = 5WT, 4HET
FDR in comb < 0.1 ; n = 221
Concordance Score: 0.96
Concordance Score: 1
Concordance Score: 0.96
male logFC
female logFC
comb logFC
E
Const vs Pseudobulk
Pvalue in Pseudobulk < 0.05; n = 209
R = 0.41
C = 0.72
logFC_psB
logFC_bulk
Nuclear vs Pseudobulk
Pvalue in Pseudobulk < 0.05; n = 208
R = 0.51
C = 0.72
logFC_psB
logFC_nuc
Synaptic vs Pseudobulk
Pvalue in Pseudobulk < 0.05; n = 214
R = 0.41
C = 0.64
logFC_psB
logFC_syn
F
Nuc DEGs per Glutamatergic module (p<0.2)
Upreg DEG count
Downreg DEG count
M1
M2
M3
M4
M5
M6
M7
M8
M9
M10
G
qPCR validation of Chd8+/5del vs Chd8WT DEGs
1/Delta Ct
Gene and Genotype
Genotype
het
wt
qPCR logFC
RNA-seq log2FC
Concordance Score: 1
Cgn-het
Cgn-wt
Crlf2-het
Crlf2-wt
Dnajc4-het
Dnajc4-wt
Egf16-het
Egf16-wt
Exon1-het
Exon1-wt
Exon11-het
Exon11-wt
Mpst-het
Mpst-wt
Oard1-het
Oard1-wt
Rec8-het
Rec8-wt
Slx2-het
Slx2-wt
Slc47a1-het
Slc47a1-wt
Slc5a5-het
Slc5a5-wt
Ttr-het
Ttr-wt
Wars2-het
Wars2-wt
Zfp438-het
Zfp438-wt

68

Figure S5: A-B) MDS plot of cortical *Chd8* mutant (A: *Chd8*$^{+/-}$, B: *Camk2a-CRE Chd8*$^{+/flox}$) and WT samples, with the the second dimension ("dim2") reflecting biological sex. C) PCA plot of cortical *Chd8*$^{+/-}$ and *Chd8*^{WT} synaptic and nuclear samples, where leading dimensions distinguish sample fraction. D) Log fold change (logFC) concordance scatterplots comparing logFC of DEGs from the combined ("comb") analysis to their logFCs in each of the sex-stratified analyses ("male", "female"). Only genes passing FDR < 0.1 or P < 0.01 in combined datasets were used for comparisons. Each row represents one of 4 bulk RNA-seq datasets: constitutive *Chd8*$^{+/-}$ ("Const"), conditional *Camk2a-CRE Chd8*$^{+/flox}$ ("Cond"), nuclear fraction of *Chd8*$^{+/-}$ ("Nuc"), and synaptic fraction of *Chd8*$^{+/-}$ ("Syn"). Plots display gene-level logFC correlations between pairs of analyses with linear regression fits and concordance scores indicating the fraction of genes regulated in the same direction. E) LogFC scatterplots comparing constitutive *Chd8*$^{+/-}$ ("Const") to pseudobulk snRNA-seq DEGs (top), nuclear fraction *Chd8*$^{+/-}$ ("Nuc") to pseudobulk DEGs (middle), and synaptic fraction *Chd8*$^{+/-}$ ("Syn") to pseudobulk DEGs. Genes were selected based on significance in pseudobulk analysis (P < 0.05) and differential expression in each respective bulk RNA-seq analysis. Pearson correlation coefficients (R) and concordance scores (C) are shown on each plot. F) Bar plots showing counts of nuclear differentially expressed genes (DEGs) per module, separated into upregulated (top) and downregulated (bottom). Enrichment was assessed using Fisher's exact test, comparing the proportion of up- vs. downregulated DEGs in each module relative to all other modules, with multiple testing correction (Benjamini-Hochberg). M1 and M7 were significantly enriched for upregulated DEGs (p*** < 0.001), while M9 was enriched for downregulated DEGs (p* < 0.05). G) Box plots showing the median 1/ΔCt (relative to GAPDH) across biological replicates for 13 constitutive *Chd8*$^{+/-}$ bulk RNA-seq DEGs. *Chd8* Exons 1 and 11 ("Exon1", "Exon 11") were included as positive controls. A Wilcoxon text showed nonsignificant differences in 1/ΔCt between *Chd8* mutants and wild-types, all 13 genes tested showed the same direction of change as RNA-seq DE analysis. Inset shows scatterplot of RNA-seq logFC versus qPCR logFC, with concordance calculated as in (D-E).